2017

Investigation of Iron(II) Autoxidation Rate And Iron Mediated Geochemical Production Of Reactive Oxygen Species At Oxic-Anoxic Interfaces

Dewamunnage Muditha Chathurangani Dias
University of South Carolina

INVESTIGATION OF IRON(II) AUTOXIDATION RATE AND IRON MEDIATED GEOCHEMICAL PRODUCTION OF REACTIVE OXYGEN SPECIES AT OXIC-ANOXIC INTERFACES

by

Dewamunnage Muditha Chathurangani Dias

Bachelor of Science
University of Colombo, 2011

Submitted in Partial Fulfillment of the Requirements

For the Degree of Doctor of Philosophy in

Chemistry

College of Arts and Sciences

University of South Carolina

2017

Accepted by:

Timothy Shaw, Major Professor

John Ferry, Committee Member

Caryn Outten, Committee Member

Alicia Wilson, Committee Member

Cheryl L. Addy, Vice Provost and Dean of the Graduate School

DEDICATION

This work is dedicated to my family who love and support me unconditionally through every chapter in my life. To my mother whose love and encouragement is a constant reminder for me to push myself to do the best in life. My father, for believing in me and always being my rock to lean on. My big brother, who I am really proud of and greatly adore. To Bruno, Marsha, Bashee and Rudy; the best pets who never fail to put a smile on my face.

ACKNOWLEDGEMENTS

First and foremost, I extend my sincere gratitude to my advisor, Dr. Timothy Shaw for his patient guidance and direction that made this dissertation a possibility. I appreciate the freedom he gave me in conducting my research and keeping me motivated through every stage of my projects. His mentoring has helped me greatly in staying focused and keeping my enthusiasm when the projects get tough. I am thankful to Dr. John Ferry, for all his advice and support given for my work and for providing insightful comments on my research papers. Furthermore, I appreciate him giving me access to his laboratory instruments which I have freely used during my Ph.D. study. I would also like to thank my committee members, Dr. Caryn Outten and Dr. Alicia Wilson for their support and invaluable advice throughout grad school work. My sincere thanks go to Dr. Daniel Reger for providing his beach house which was used as the sampling station at Folly Beach in Charleston. I am deeply thankful to Dr. Willard Moore and Dr. Claudia Benitez-Nelson for providing access to the RaDeCC system to analyze the radium samples.

I want to thank my friend and lab mate, Dr. Justin Copeland whose early research laid the foundation for some of the work presented here and for mentoring me during the early stages of my graduate career. Also, my thanks go to Lauren Reince, the excellent undergraduate researcher for her assistance in the lab.

I would like to thank past and present Ferry group members; Dr. Shengnan Meng, Benson Solomon, Meagan Smith, Fan Wang and Sam Putnam for their friendship and generously accommodating me in using their lab equipment and for helping me drag seawater carboys across Folly Beach. Also, I would like to thank Xiangming 'Sunny' Shi for her support in radium sample preparation and analysis. I greatly appreciate Dr. Randima Galhenage, Dr. Sahan Salpage, Dr. Gaya Elpitiya and Mr. Malinda Witharana for their support in helping me settle and feel at home when I first moved to South Carolina. I am thankful to all my wonderful friends back in Sri Lanka for their love and for throwing awesome reunion parties every time I visit. Further, I want to thank all my friends here at USC for their support and encouragement. The get-togethers and the night-outs certainly made my experience at USC more memorable.

I extend my sincere thanks to all college professors and teachers who have inspired and guided me throughout the years. Further, my thanks go to everyone at USC who have helped me in many ways and encouraged me during my studies including the Chemistry department staff, International Student Services and Ms. Jackie and the coffeeshop crew for their warm greetings every morning and of course the coffee.

Finally, I want to thank my parents and my brother for their unconditional love that has got me going even in the toughest times. I am forever grateful for their sacrifices and support that have shaped me to be the person I am today.

ABSTRACT

Biogeochemical cycles in ecosystems regulate the flow of energy between reduced species (typically carbon compounds) and a variety of oxidants via both biotic and abiotic reactions. A key class of chemical compounds that can link these cycles through abiotic pathways are Reactive Oxygen Species (ROS). The production of ROS via photochemical pathways is well known. More recently, the non-photochemical production of ROS via the one electron oxidation of ferrous iron (Fe(II)) by dioxygen (O_2) has been detected in a range of environments. The oxidation of Fe(II) initiates a pathway that generates an array of ROS as Fe is cycled between Fe(II) and Fe(III) oxidation states. This dissertation presents studies to investigate the oxidation kinetics of Fe(II) and its role in producing and maintaining ROS at oxic-anoxic boundaries.

The determination of the rate constant for the reaction of Fe(II) and dioxygen is a challenge due to the difficulty in isolating the reaction from an assortment of simultaneous reactions involved in the Fe cycling process. The second order reaction rate evaluated using a competition kinetics method against a series of Fe-binding ligands was determined to be within $7x10^8$- $2x10^9$ $M^{-1}s^{-1}$. This fast reaction kinetics suggest that in natural environments, oxic-anoxic interfaces can trigger the rapid generation of ROS.

Historically salt marshes are associated with rapid primary production of plant material but low subsequent decomposition due to physical limitation of oxygen availability. Oxygen transport into carbon rich sediments is thought to be limited by low

permeability in the fine-grained marsh sediments. Physical characteristics arising from marsh grass rhizosphere and benthic burrows can greatly alter the flow dynamics enhancing the advective flow of oxygen rich water into marsh sediment containing reduced species such as Fe(II). Radium tracer studies based on $^{228}Th/^{224}Ra$ disequilibrium were employed to assess the water exchange through a coastal marsh system. The greater flow and heightened mixing efficiency promote the trapping of particle phases and the transport of oxygen and other terminal electron acceptors to aid the organic carbon oxidation.

The production of ROS in the absence of light was verified in the organic carbon rich sediment around the rhizophere of the common marsh grass, *Spartina alterniflora*. Metastable mixtures of Fe(II), O_2 and ROS were measured over several seasons. This finding indicates an abiotic pathway for ROS generation and a subsequent ROS mediated mechanism for the degradation of organic carbon in aquatic environments. Ultimately, these processes affect the carbon burial capacity and the export of carbon flux to the oceans making these ecosystems key players in regulating global carbon budgets.

Table of Contents

LIST OF TABLES

LIST OF FIGURES

LIST OF ABBREVIATIONS

Bipyr .....2,2'-Bipyridine

DO.....Dissolved Oxygen

dpm .....disintegrations per minute

DTPA……..……Diethylenetriaminepentaacetic acid

Fz..... Ferrozine

GF/F .....Glass Fiber Filter

HEPES .....4-(2-Hydroxyethyl)piperazine-1-ethanesulfonic acid

MCLA ..... 2-methyl-6-[p-methoxyphenyl]-3,7-dihydroimidazo[1,2-a]pyrazin-3-one

NOM .....Natural Organic Matter

Phen.....1,10-Phenanthroline

PMT .....Photomultiplier tube

ppt .....Parts per thousand

RaDeCC .....Radium Delayed Coincidence Counter

ROS.....Reactive Oxygen Species

CHAPTER 1

A COMPETITION KINETICS STUDY FOR THE EVALUATION OF THE RATE CONSTANT FOR THE FE(II) AUTOXIDATION REACTION

1.1 Abstract

The second order rate constant for the Fe^{2+} reaction with dioxygen reported in literature shows significant disparity. The presence of a number of parallel second order reactions in the iron cycling process makes it a challenge to isolate the Fe^{2+}-O_2 reaction and determine the rate constant using kinetic models. Here, results from a competition kinetics study to determine the value of the Fe^{2+} oxidation rate constant are presented. When Fe^{2+} is introduced to an oxygenated system containing an Fe^{2+} chelator, the ligand and dioxygen simultaneously compete to react with Fe^{2+}. When no interfering side reactions are present, such a system can be manipulated to establish the Fe^{2+} oxidation rate constant, using the well-known formation rate constants for Fe^{2+}-ligand complexes as references. Here, phosphate was used to selectively complex Fe^{3+} and inhibit the regeneration of Fe^{2+}. 1,10-Phenanthroline and 2,2'-Bipyridine were used as reference compounds and the fraction of Fe^{2+} reacted with the ligand was determined spectrophotometrically. The calculated rate constant falls in the range of $1.3x10^7 – 1.9x10^8$ $M^{-1}s^{-1}$. This is several orders of magnitude higher than previously reported values and is comparable to the reaction rate constant of the back reaction between Fe^{3+} and superoxide.

1.2 Introduction

For decades, the efforts to measure the oxidation rate of Fe^{2+} have been a challenge due to the complicated nature of the iron cycling process. This process is comprised of several simultaneous second order reactions, making the isolation of the initial oxidation step (reaction 1.1 below) a difficult task. In order to minimize the complications imposed by the back reaction, many studies have been carried out at nanomolar levels of iron.[1-5]

However, even at such levels, the back reaction can still be significant in regenerating Fe^{2+}. Unless caution is taken to block the back reaction to negate its impact on the Fe^{2+} oxidation, an artefact is introduced into the calculations. Different species such as Br^-, Cl^- or CO_3^{2-} are commonly introduced as sources to outcompete iron and react with superoxide. However, the introduction of such species complicates the system matrix, leading to the formation of various iron species that react at different reaction rates with dioxygen and other oxidants. Since, the exact reaction rate constants for all these reactions are unknown, computing the Fe^{2+} oxidation rate constant becomes complex and often lead to circular references.

The cycling of iron between its Fe^{2+} and Fe^{3+} oxidation states plays a significant role in iron solubility and bioavailability in aquatic environments.[6-10] The one-electron oxidation of Fe^{2+} to Fe^{3+} (reaction 1.1 below) is the initial step in the net oxidation and subsequent removal of Fe from the dissolved phase. This reaction initiates the production of reactive oxygen species (ROS) as shown in reactions 1.2-1.4 below. However, the resultant Fe^{3+} can be rapidly regenerated back to Fe^{2+} through reaction of Fe^{3+} with a number of possible electron donors including ROS and reduced sulfur species.[11-20] In aquatic systems, the persistence of the cycle is limited by the availability of electron donors and/or the precipitation of Fe^{3+} as soluble complexes. The residence time of Fe^{2+} in aquatic systems is a function of the relative net rates of the reactions within the cycle. Reactions 1.1- 1.4 represent the proposed catalytic mechanism for the redox cycling of iron species with ROS.

$$Fe^{2+}+O_2 \leftrightharpoons Fe^{3+}+O_2^- \qquad \text{reaction 1.1}$$

$$Fe^{2+}+O_2^- \rightarrow Fe^{3+}+H_2O_2 \qquad \text{reaction 1.2}$$

$$Fe^{2+}+H_2O_2 \rightarrow Fe^{3+}+HO^{\cdot} \qquad \text{reaction 1.3}$$

$$Fe^{2+}+HO^{\cdot} \rightarrow Fe^{3+}+HO^{-} \qquad \text{reaction 1.4}$$

While numerous studies have been conducted to examine various aspects of this redox process, the rate of the reaction between Fe^{2+} and molecular oxygen (reaction 1.1) is not well constrained. This reaction is the critical initiating step of the process and proper understanding of its thermodynamic and kinetic characteristics are of high importance to explain and predict how the iron redox cycling and the ROS generation would proceed in natural systems. The reported second order rate constants for the reaction between Fe^{2+} and dioxygen (forward reaction 1.1) vary between 0.058 – 170 $M^{-1}s^{-1}$.[21-25] Pulse radiolytic studies report a rate constant of $1.5x10^8$ $M^{-1}s^{-1}$ for the reverse reaction 1 which was re-assessed and shown to be valid at seawater pH.[20,26] These rates should heavily favor the reverse reaction over the forward reaction, suggesting Fe^{2+} should be the more kinetically stable species in aqueous medium. However, the opposite appears to hold true as the one electron oxidation of Fe^{2+} under many oxygenated conditions yields Fe^{3+} as the more stable of the two species. Thus, there is a discrepancy between the reported reaction rates and what is practically observed for reaction 1.1. For Fe^{3+} to be the more kinetically stable species in a system, the magnitude of the rate limiting forward reaction 1.1 should be comparable to that of the reverse reaction.

The widely-used method for investigating the kinetics of the iron oxidation reaction has been to monitor the loss of Fe^{2+} over time under different experimental conditions and model the rate constant as a fitted parameter of a kinetic model.[2,21,27] Here, it is important to establish first order reaction kinetics with respect to one reactant so that the array of reactions can be integrated together and ultimately isolate the Fe^{2+} oxidation reaction by

dioxygen and elucidate its reaction kinetics. If such (pseudo) first order conditions are not met, it can introduce an artefact to the rate calculations. Moreover, as the number of kinetic parameters incorporated in the model increase, the error introduced through the uncertainties in published rate constants can have a significant effect on the model outcome. Most of the early kinetic studies at micro molar levels of Fe^{2+} disregard the impact of the reverse reaction. Studies by Burns *et.al.* report that Fe^{2+} concentrations greater than 4 µM leads to iron cycling up to 10 – 2200 times before its net oxidation.[16,17] Regeneration of Fe^{2+} via the reaction of Fe^{3+} with superoxide would lead to underestimation of the rate constant for the forward reaction.

An alternative approach for investigating the kinetics of a fast reaction is the method of competition kinetics. This is a well-established method where an unknown reaction is tested together with a similarly fast reaction with a known rate constant, competing for the same substrate.[28-37] Since the rate of the unknown reaction is measured relative to a reference reaction it eliminates the need for direct monitoring of the unknown reaction.

When two reactants (A and B) compete for the same substrate (X), the fraction of X reacting with A can be given by the following expression (Eq 1.1).

$$\text{fraction of X reacting with A} = \frac{k_1[A][X]}{(k_1[A][X]+k_2[B][X])} \qquad \text{Eq 1.1}$$

where k_1 and k_2 are the respective reaction rate constants for A and B with X.

When the reaction kinetics of one of the reactants is known, it can be treated as a reference compound. By measuring the fraction of the substrate reacting with the reference

probe, either as the formation of the product or the disappearance of the reference compound, the rate constant for the second reaction can be calculated.

The competition kinetics method for systems involving iron chemistry has been used to elucidate Fenton chemistry, i.e. the reaction between Fe^{2+} and H_2O_2 and the consequent oxidation of organic compounds by hydroxyl radicals.[38-40] A series of studies by Kolthoff and Medalia assessed the stoichiometry of Fe^{2+} / H_2O_2 reaction in the presence of different organic compounds.[41,42] These experiments conducted in the absence of oxygen showed Fe^{2+} and H_2O_2 competing for $^{\cdot}OH$. In the presence of oxygen, the kinetics of the reaction system was complicated as oxygen outcompeted H_2O_2 to react with Fe^{2+}, disrupting the predicted stoichiometric outcome for the Fenton reaction. While these studies were not focused on calculating rate constants, they are early examples where competition reaction kinetics has been employed to explore the differences in relative reactivities of reactions in the iron cycling process.

To the best of our knowledge no previous studies have been reported where a competition kinetic approach has been employed to evaluate the intrinsic value of the rate constant for the Fe^{2+} - dioxygen reaction. Here, a study conducted in an effort to assess this second order rate constant using a two-competing reaction system is presented. Different ligands can form intensely colored complexes upon reacting with Fe^{2+} that can be quantified using spectrophotometry. The rate constants for these reactions are well established in literature, thus can be used as reference compounds in a competition kinetic setup. For this study, separate experiments were conducted with each of two ligands, 1,10-Phenathroline and 2,2'-Bipyrindine. Experimental conditions were manipulated to eliminate contributions of the back reaction to measured rates, e.g. addition of PO_4^{3-} to

complex the Fe^{3+}. The goal was to generate a system that can be modeled as a two-reaction system where the ligand and dioxygen compete simultaneously for Fe^{2+}.

1.3 Experimental Methods

Materials

Iron(II) chloride, anhydrous (99.5%) was purchased from Alfa Aesar. 1,10-Phenanthroline (> 99%) was acquired from Acros Organics and 2,2'-Bipyridine from JT Baker. HEPES (≥ 99.5%) was obtained from Sigma-Aldrich. Sodium phosphate monobasic (100%) and Sodium phosphate dibasic heptahydrate (98.9%) were purchased from Fisher Scientific. All solutions were prepared in 18 $M\Omega cm^{-1}$ water. For Fe(II) stock solutions, water was boiled for one hour and kept under nitrogen to maintain oxygen free conditions.

Analytical Methods

Fe(II) was quantified colorimetrically using 1,10-Phenanthroline [43-45] and 2,2'-Bipyridine [46-48] using a Spectramax M5 UV-Vis scan microplate reader (Table 1.1). The oxygen concentrations of the solutions were measured using a four-channel fiber optic oxygen meter (Pyroscience Firesting O2 FSO2-0x) coupled with bare fiber minisensors (OXB430). A Thermo Scientific Orion 5-star pH meter was used to make pH adjustments.

Fe^{2+} oxidation experiments

Solutions buffered at pH 7.8 (25 mM HEPES) were spiked with Fe^{2+} to reach an initial concentration of 25 µM. Samples were withdrawn from the reactor at different time points and the Fe^{2+} was quantified using 1,10-Phenanthroline and 2,2'-Bipyridine (ligand concentration = 1 mM). Experiments were run in triplicate for each ligand.

Competition kinetics experiments

Phosphate solutions of varying concentration (as total phosphate; 5 – 900 mM) were prepared using $NaH_2PO_4.H_2O$ and $Na_2HPO_4.7H_2O$ and pH adjusted to 7.8. At each phosphate concentration, a series of solutions were prepared by varying the ligand concentration (1,10-Phenanthroline or 2,2'-Bipyridine) in the range 75 – 2000 µM. To initiate the reaction, each vial containing the ligand and phosphate was spiked with Fe^{2+} to reach a concentration of 25 µM. The concentration of the colored complex formed was determined spectrophotometrically. Since the Fe^{2+} reaction with dioxygen does not produce any colored species, the fraction of Fe^{2+} reacting with the chelator can be calculated. All experiments were run in triplicates.

Multifactorial Design Experiments

To investigate the possibility of interactions between ligands, high levels of phosphate and Fe^{3+} that would introduce a defect to the observed outcome, 3-factor Box-Wilson central composite designs were used to examine the relationship between phosphate (pH 7.8), Fe^{3+} and each ligand (Table 1.2) on the formation of the Fe(II)-ligand complexes. Using Design Expert software, the parameter space was set by allotting the concentration range for each variable at five levels. The overall matrix contained 20 experimental conditions with 6 replicates at the center point and 3 replicates for all other conditions summing to a total of 48 individual experiments for a given ligand. A single matrix was performed for each ligand; 1,10-Phenanthroline and 2,2'-Bipyridine. To initiate the reaction, a 25 µM Fe(II) spike was made to each reactor and the amount of Fe(II)-ligand complex formed was determined spectrophotometrically.

1.4 Results

In the oxygenated solutions, Fe^{2+} was rapidly oxidized over time and the observed decay was comparable with both ligands (Figure1.1). The oxidation was first order with respect to Fe^{2+} and the calculated rate constant (k_{obs}) for each ligand series resulted in similar values (Figure 1.2) with an average k_{obs} of 0.0062(±0.0004) s^{-1}. With the measured oxygen concentration of 260 µM, this correspond to a second order rate constant of 23.9 (±1.5) $M^{-1}s^{-1}$.

In the competitive kinetics experiments, at all phosphate concentrations, increasing the ligand concentration gradually increased the fraction of Fe^{2+} reacting with the ligand before completely outcompeting dioxygen and reaching a plateau point (Figure 1.3). Under conditions where Fe^{3+} is rapidly scavenged by the reaction with PO_4^{3-}, equation 1.1 becomes a competitive reaction system between O_2 and ligand (L) (Eq 1.2). This can be rearranged to plot the data such that the second order rate constant for Fe^{2+} autoxidation is represented in the slopes of plots between 1/fraction of Fe^{2+} reacting with the ligand and $1/[ligand]^3$ (Eq 1.3). The validity of the method is tested by the linearity of this relationship. The solution oxygen concentrations measured were at saturated levels (~260 µM) during the course of the experiment. This ~10-fold excess of dioxygen over Fe^{2+} ensures that the Fe^{2+} oxidation reaction is first order with respect to Fe^{2+}. Since the complexation rate (k_L) for each ligand is known (Table 1.1), the reaction rate for Fe^{2+} oxidation (k_{ox}) can be calculated.

$$\text{fraction of } Fe^{2+} \text{ reacting with ligand} = \frac{k_L[L]^3[Fe^{2+}]}{(k_L[L]^3[Fe^{2+}]+k_{ox}[O_2][Fe^{2+}])} \quad \text{Eq 1.2}$$

when, the fraction of Fe^{2+} reacting with ligand=X

$$\frac{1}{X} = 1 + \frac{k_{ox}[O_2]}{k_L} \cdot \frac{1}{[L]^3}$$ Eq 1.3

The data plotted according to equation 3 was linear in the considered range (Figure 1.4) and an absolute value of the second order rate constant for Fe^{2+} autoxidation for each phosphate level was calculated using the slopes of each graph.

For both ligands, the calculated second order rate constant increased with increasing phosphate until it plateaued. With 1,10-Phenanthroline, for total phosphate concentrations over 0.3 M, a rate constant of 1.9(±0.3) $x10^8$ $M^{-1}s^{-1}$ was calculated (Figure 1.5). The value computed using 2,2'-Bipyridine was 1.3(±0.2) $x10^7$ $M^{-1}s^{-1}$, recorded for total phosphate over 0.5 M (Figure 1.6). Thereby, the second order rate constant for Fe^{2+} reaction with O_2 was calculated to be in the range between $1.3x10^7$ – $1.9x10^8$ $M^{-1}s^{-1}$.

The relationship between the Fe^{2+}-ligand complex formed and the three variables (ligand, phosphate and Fe^{3+}) was evaluated by fitting a quadratic equation to a response surface describing the observable versus the three factors and their possible interactions. These quadratic expressions for all three matrices include the three factors (x_1, x_2, x_3), linear coefficients for each term (β1, β2, β3), squared coefficients (β11, β22, β33), cross product coefficients (β12, β23, β13) and a constant term (β0) (Eq 1.4).

$$[Fe^{2+}L_3] = \beta_0 + \beta_1 x_1 + \beta_2 x_2 + \beta_3 x_3 + \beta_{11} x_1^2 + \beta_{22} x_2^2 + \beta_{33} x_3^2 + \beta_{12} x_1 x_2 + \beta_{13} x_1 x_3 + \beta_{23} x_2 x_3$$

Eq 1.4

These quadratic expressions were simplified by including only the factors that are statistically significant ($p \leq 0.05$) for the outcome (Eqs 1.5 and 1.6). All β values were modeled by the Design Expert software and the ratio between the sum of squares for each

factor and the sum of squares for the model is used to determine the percentage impact of each factor towards the outcome (Table 1.3-1.8). Both response surfaces correlated well with the observed outcome with r^2 values of 0.891(Fe-Phen) and 0.950 (Fe-Bipyr).

$$[Fe^{2+}Phen_3]=\beta_0+\beta_1x_1+\beta_2x_2+\beta_3x_3+\beta_{11}x_1^2 \quad \text{Eq 1.5}$$

$$[Fe^{2+}Bipyr_3]=\beta_0+\beta_1x_1+\beta_2x_2+\beta_3x_3+\beta_{11}x_1^2+\beta_{33}x_3^2+\beta_{13}x_1x_3+\beta_{23}x_2x_3 \quad \text{Eq 1.6}$$

Based on these calculations, for the formation of Fe^{2+}-1,10-Phenanthroline complex, [Phen] accounted for 45% of the model while $[PO_4^{3-}]$ (21%) and $[Phen]^2$ (22%) also made significant impacts. $[Fe^{3+}]$ played a minor role accounting for only 7% of the model. [Bipyr] (45%) and $[PO_4^{3-}]$ (26%) were the two major factors impacting the model for Fe-2,2'-Bipyridine complex formation. Five other terms were deemed to be minor contributors with each accounting for less than 10% of the model. These factors were $[Fe^{3+}]$, $[Bipyr]^2$, $[Fe^{3+}]^2$, $[Bipyr\text{-}PO_4^{3-}]$ and $[PO_4^{3-}\text{-}Fe^{3+}]$. The sign of β_x indicate the direction of the action of each factor with positive coefficient indicating an increase in the ligand complex formation and a negative coefficient indicating a decrease in the complex formation. For all three matrices, ligand concentration had a positive coefficient while that for PO_4^{3-} concentration was negative.

1.5 Discussion

The Fe^{2+} oxidation experiments were conducted in oxygen saturated solutions, where oxygen was never limiting, resulting in first order oxidation conditions with respect to Fe^{2+}. The complexation reactions of the ligands with Fe^{2+} are essentially competition reactions between dioxygen and ligand. When the ligand is present in high enough

concentrations, it outcompetes oxygen to bind all available Fe^{2+}. In the absence of such competition, the observed oxidation kinetics should yield similar results regardless of the complexing ligand. This is evident by the resultant rate constants (k_{obs}) calculated, using the Fe^{2+} decays quantified using the two different ligands.

When a ligand is present at a level where dioxygen in the system can successfully compete with the ligand for the reaction with Fe^{2+}, a competition reaction system is established. Here, in contrast to the earlier case, the level of competition by each ligand is dependent on the formation rate of the Fe^{2+}-ligand complex. This concentration dependent competition can be utilized to deduce an unknown rate entity relative to a well-known reaction rate. This approach was necessary to test the hypothesis that the Fe^{2+} reaction with dioxygen is comparable in magnitude, to the reverse reaction of Fe^{3+} reacting with superoxide ($1.5x10^{8}\ M^{-1}s^{-1}$). The hypothesis reflects the kinetic stability of Fe^{3+} under oxic conditions. For the two ligands 1,10-Phenanthroline and 2,2'-Bipyridine the stability constants are $3x10^{21}$ and $1.21x10^{17}$ $M^{-3}s^{-1}$ respectively.[43,47] As evident by these high stability constants, once these ligands complex with Fe^{2+}, the complexes are very stable in aqueous media. Fe^{3+} has been observed to form Fe^{3+}-Phen complexes causing an interference for the colorimetric determination of Fe^{2+} by 1,10-Phenanthroline. However, this interference has been found to be significant only when Fe^{3+} is present at millimolar levels.[49]

According to the reaction rates for superoxide disproportionation[50], as the fraction of $O_2^{\cdot-}$ increases, the disproportionation becomes less important, and the Fe^{3+} reaction with superoxide becomes more significant. Therefore, phosphate was used as an Fe^{3+} chelator to impede the effects of the back reaction. Phosphate competes with superoxide for Fe^{3+},

and when present in adequate amounts it outcompetes superoxide to completely block Fe^{2+} regeneration by the back reaction. Thereby, a two-competing reaction system is established, where dioxygen competes with a chelating ligand for Fe^{2+}. Hence, for the accurate measurement of the oxidation rate constant, the reverse reaction should be blocked to prevent Fe^{3+} from regenerating Fe^{2+}. In our study, this was achieved by employing phosphate as the Fe^{3+} scavenger.

The second order rate constant calculated using the two separate ligands agree well with each other ranging from $1.3x10^{7}$ – $1.9x10^{8}$ $M^{-1}s^{-1}$. The magnitude of this range is on the order of the rate of the back reaction of Fe^{3+} with superoxide. Thus, Fe^{2+} autoxidation should successfully compete with the back reaction to ultimately drive the reaction scheme forward to make Fe^{3+} the more stable species in the system. Due to the uncertainty surrounding the reported rate constants in literature, it is difficult to compare our results with a reference value. However, the experimental range obtained in this study is several orders of magnitude greater than previously reported numbers.

The phosphate concentration at the graph plateauing point (Figures 1.5 and 1.6) is assumed to be the phosphate concentration required to effectively bind and prevent Fe^{3+} from taking part in the cycling process such that further input of the scavenger produces no significant change to the Fe^{2+} autoxidation rate. At the reaction pH (7.8) the dominant species of phosphate are $H_2PO_4^-$ and HPO_4^{2-}. Therefore, while millimolar levels of total phosphate concentrations used in the experiments, PO_4^{3-}, existed only at low micro molar levels. Out of the two ligands, 2,2'-Bipyridine required a higher phosphate concentration to completely sequester Fe^{3+}. Compared to 1,10-phenanthroline, 2,2'-Bipyridine has a slower reaction rate with Fe^{2+}. Therefore, for a given set of conditions, the fraction of Fe^{2+}

reacting with O_2 is higher for 2,2'-Bipyridine. Consequently, this leads to a higher generation of Fe^{3+}, requiring a larger amount of phosphate to complex it.

A third set of experiments was run parallel to deduce the oxidation rate constant using ferrozine as the Fe^{2+} binding ligand (Figures 1.7-1.11, Tables 1.9-1.11). However, this proved to be problematic due to the comparatively lower reaction rate of ferrozine with Fe^{2+} ($k_{ferrozine} = 3.0x10^{11}\ M^{-1}s^{-1}$).[51] Compared to the other two ligands, this lower binding rate makes the competition by dioxygen more prominent in the presence of ferrozine leading to higher levels of Fe^{3+} and superoxide to be generated in the medium. Thereby, the amount of phosphate required to completely block the back reaction in the presence of ferrozine proved to be too high, that it exceeded the limits of complete phosphate solubility. Furthermore, the charged nature of ferrozine requires amending for ionic strength effects. At such elevated phosphate concentrations, the ionic strengths of the solutions are too high to make reasonable adjustments for activity coefficients. Therefore, we believe the results obtained using ferrozine as the reference are unreliable and were not included in the rate constant calculations.

The phosphate induced acceleration in Fe^{2+} oxidation has been observed under different conditions irrespective of the matrix constituents.[16,17] In addition to phosphates, any ligand that masks Fe^{3+} and blocks the back reaction can prompt rapid Fe^{2+} oxidation. In natural waters, hydroxides, carbonates and various organic ligands can act as Fe^{3+} chelators resulting in the accelerated rates of Fe^{2+} oxidation observed in oxic-anoxic interfaces. [16-19, 23-24, 52]

ANOVA results from the multivariate experiments show that for both ligands, the formation of the Fe^{2+}-ligand complex is predominantly a function of the ligand and the

phosphate concentrations. Interactions between ligand and Fe^{3+} or ligand and phosphate were determined to have minimal effect on the observable with impacts typically under 10%. This shows that except for the ligand and dioxygen competing for Fe^{2+}, other interactions between participating species can be considered to be negligible for the formation of Fe^{2+}-ligand complex. Therefore, it is reasonable to treat the system as a two-reaction system competing for Fe^{2+}. The validity of the competition kinetics technique applied to the system is further evidenced by the linear correlation exhibited by the data following equation 3 (Figure 1.4).

The impact on the outcome (i.e. the Fe^{2+}-ligand complex formation) was positive for the ligand concentration, which is expected since increasing levels of the ligand promote the binding of Fe^{2+}. For phosphate, the impact was negative. When phosphate complexes Fe^{3+}, the cycling of iron is hindered, increasing the net iron oxidation. In such case, the relative effectiveness of the competition by dioxygen is increased leading to a lower fraction of Fe^{2+} reacting with the ligand.

1.6 Conclusion

The competition kinetics method was used to assess the reaction rate for the reaction of Fe^{2+} with dioxygen at circumneutral pH. As the fraction of $O_2^{\cdot -}$ increases, the disproportionation of superoxide becomes less important, and the Fe^{3+} reaction with superoxide becomes more significant. Therefore, phosphate was used as an Fe^{3+} chelator to impede the effects of the back reaction. Phosphate competes with superoxide for Fe^{3+}, and when present in adequate amounts it outcompetes superoxide to completely block Fe^{2+} regeneration by the back reaction. Thereby, a two-competing reaction system is

established, where dioxygen competes with a chelating ligand for Fe^{2+}. The calculated rate constant falls within the range $1.3x10^{7} – 1.9x10^{8}$ $M^{-1}s^{-1}$. This is several orders of magnitude greater than what has been previously determined with kinetic modeling approaches. This range is reasonable to suggest that Fe^{2+} can successfully compete with the Fe^{3+}-superoxide reaction in order for Fe^{3+} to be the more stable species under oxic conditions.

Table 1.1: Absorption maxima, molar absorptivity and the complexation rate with Fe^{2+} for the two ligands used in the competitive kinetics study.

Ligand	λ_{max} (nm)	Molar absorptivity ($M^{-1}cm^{-1}$)	Complexation rate with Fe^{2+} ($M^{-3}s^{-1}$)
1,10-Phenanthroline	508	11100	$2.9(\pm0.5)\ x10^{16}$
2,2'-Bipyridine	522	8650	$1.4(\pm0.2)\ x10^{13}$

Table 1.2: Parameter space for the central composite experimental design
The respective ligand for each matrix was either 1,10-Phenanthroline or 2,2'-Bipyridine.

Factor (units)	**Factor concentration levels**				
Coded factor levels	-2	-1	0	1	2
$[PO_4^{3-}]_{total}$ (mM)	5	186.4	452.5	718.6	900
[ligand] (µM)	50	465.2	1037.5	1609.8	2000
$[Fe^{3+}]$ (µM)	0	50.7	125	199.3	250

Table 1.3: Experimental conditions and the observed response for 1,10-Phenanthroline matrix.

Run	Factor 1 A: [1,10-Phen] (µM)	Factor 2 B: $[PO_4]^{3-}_{total}$ (mM)	Factor 3 C: $[Fe^{3+}]$ (µM)	Response $[Fe\text{-}(Phen)_3]$ (µM)	Response RSD (%)
1	2000.0	452.5	125.0	2.78E-05	5.0
2	1609.8	718.6	199.3	2.58E-05	2.6
3	465.2	186.4	199.3	2.58E-05	0.1
4	1037.5	452.5	125.0	2.64E-05	3.5
5	1037.5	452.5	125.0	2.59E-05	3.4
6	1609.8	186.4	50.7	2.42E-05	7.4
7	1037.5	452.5	125.0	2.53E-05	3.5
8	1609.8	718.6	50.7	2.34E-05	17.6
9	465.2	186.4	50.7	2.15E-05	7.1
10	1037.5	452.5	125.0	2.62E-05	2.8
11	1037.5	452.5	125.0	2.49E-05	3.6
12	75.0	452.5	125.0	1.29E-05	13.3
13	1037.5	452.5	125.0	2.81E-05	3.2
14	465.2	718.6	50.7	2.06E-05	3.6
15	465.2	718.6	199.3	1.93E-05	16.7
16	1037.5	5.0	125.0	3.07E-05	2.9
17	1037.5	452.5	0.0	2.35E-05	3.8
18	1609.8	186.4	199.3	2.95E-05	3.7
19	1037.5	452.5	250.0	2.65E-05	9.5
20	1037.5	900.0	125.0	2.15E-05	4.1

Table 1.4: Experimental conditions and the observed response for 2,2'-Bipyridine matrix.

Run	Factor 1 A: [2,2'-Bipyr] (µM)	Factor 2 B: $[PO_4]^{3-}_{total}$ (mM)	Factor 3 C: $[Fe^{3+}]$ (µM)	Response $[Fe\text{-}(bipyr)_3]$ (µM)	Response RSD (%)
1	1037.5	452.5	125.0	2.14E-05	2.9
2	1037.5	452.5	125.0	2.42E-05	3.0
3	75.0	452.5	125.0	6.32E-06	10.7
4	1037.5	452.5	125.0	2.22E-05	5.6
5	465.2	186.4	199.3	2.33E-05	1.4
6	465.2	718.6	50.7	1.00E-05	22.2
7	465.2	718.6	199.3	1.41E-05	16.7
8	1037.5	900.0	125.0	1.70E-05	1.9
9	1609.8	718.6	199.3	1.62E-05	2.0
10	1609.8	186.4	50.7	2.43E-05	13.1
11	1037.5	452.5	125.0	2.21E-05	1.6
12	1037.5	452.5	250.0	2.17E-05	5.3
13	1037.5	452.5	125.0	2.21E-05	2.8
14	1609.8	186.4	199.3	3.08E-05	4.1
15	1609.8	718.6	50.7	2.42E-05	3.0
16	1037.5	452.5	125.0	1.94E-05	1.7
17	1037.5	452.5	0.0	1.44E-05	2.3
18	1037.5	5.0	125.0	2.93E-05	1.3
19	465.2	186.4	50.7	1.47E-05	16.0
20	2000.0	452.5	125.0	2.47E-05	1.3

Table 1.5: Estimates and hypothesis tests for the parameters of the quadratic model fitted to the data for the concentration of the Fe^{2+}-$(Phen)_3$ complex formed.

Parameter	βx key	Coefficient estimate	Standard Error	F Value	p-value-Prob > F	% impact
β0	intercept	26.12	0.740			
β1	1,10-Phen	2.98	0.491	36.93	1.19E-4	45.41
β2	PO_4^{3-}	-2.00	0.491	16.77	2.16E-3	20.62
β3	Fe^{3+}	1.16	0.491	5.61	3.93E-2	6.91
β12	[Phen]-[PO_4^{3-}]	0.36	0.641	0.31	0.59	0.38
β13	[Phen]-Fe^{3+}	0.57	0.641	0.78	0.40	0.96
β23	[PO_4^{3-}]-Fe^{3+}	-1.06	0.641	2.75	0.13	3.38
β11	$[Phen]^2$	-2.01	0.478	17.79	1.78E-3	21.87
β22	$[PO_4^{3-}]^2$	0.01	0.478	5.26E-4	0.98	6.47E-4
β33	$[Fe3+]^2$	-0.39	0.478	0.66	0.43	0.82

Table 1.6: Estimates and hypothesis tests for the parameters of the quadratic model fitted to the data for the concentration of the Fe^{2+}-$(bipyr)_3$ complex formed.

Parameter	βx key	Coefficient estimate	Standard Error	F Value	p-value-Prob > F	% impact
β0	intercept	21.86	0.767			
β1	2,2'-Bipyr	4.71	0.509	85.51	3.24E-06	44.67
β2	PO_4^{3-}	-3.61	0.509	50.24	3.34E-05	26.24
β3	Fe^{3+}	1.71	0.509	11.26	7.30E-3	5.88
β12	Bipyr-[PO_4^{3-}]	-0.11	0.664	0.029	0.87	0.015
β13	[Bipyr]-Fe^{3+}	-1.79	0.664	7.21	0.023	3.77
β23	[PO_4^{3-}]-Fe^{3+}	-2.38	0.664	12.79	5.05E-3	6.68
β11	$[Bipyr]^2$	-2.05	0.495	17.07	2.04E-3	8.92
β22	$[PO_4^{3-}]^2$	0.65	0.495	1.73	0.22	0.91
β33	$[Fe3+]^2$	-1.15	0.495	5.35	0.0432	2.79

Table 1.7: ANOVA for the response surface generated by the quadratic model fitted to the data for Fe-$(Phen)_3$ complex formation.

Source	Squares	df	Square	Value	Prob > F	
Model	267.4487	9	29.71652	9.036442	0.000964	significant
Residual	32.8852	10	3.28852			
Lack of Fit	26.63062	5	5.326124	4.257778	0.068902	not significant
Pure Error	6.254582	5	1.250916			
Cor Total	300.3339	19				
Std. Dev.	1.813428		R-Squared	0.890505		
Mean	24.49013		Adj R-Squared	0.791959		
C.V. %	7.404728		Pred R-Squared	0.291619		
PRESS	212.7509		Adeq Precision	12.28123		

Table 1.8: ANOVA for the response surface generated by the quadratic model fitted to the data for Fe-$(bipyr)_3$ complex formation.

Source	Squares	df	Mean Square	Value	Prob > F	
Model	677.0533	9	75.22815	21.27165	2.22E-05	significant
Residual	35.36545	10	3.536545			
Lack of Fit	23.07626	5	4.615252	1.87777	0.252967	not significant
Pure Error	12.28919	5	2.457837			
Cor Total	712.4188	19				
Std. Dev.	1.88057		R-Squared	0.950359		
Mean	20.12113		Adj R-Squared	0.905681		
C.V. %	9.346248		Pred R-Squared	0.701957		
PRESS	212.3314		Adeq Precision	16.46127		

Table 1.9: Experimental conditions and the observed response for Ferrozine matrix.

Run	Factor 1 A: [Ferrozine] (µM)	Factor 2 B: $[PO_4]^{3-}_{total}$ (mM)	Factor 3 C: $[Fe^{3+}]$ (µM)	Response $[Fe\text{-}(Ferrozine)_3]$ (µM)	Response RSD (%)
1	465.2	718.6	50.7	2.53E-06	6.7
2	1609.8	186.4	199.3	2.41E-05	3.9
3	1037.5	452.5	125.0	1.32E-05	1.3
4	1037.5	452.5	125.0	1.17E-05	10.0
5	1037.5	900.0	125.0	8.01E-06	4.1
6	1037.5	452.5	125.0	1.18E-05	3.5
7	1609.8	186.4	50.7	2.28E-05	8.9
8	1037.5	452.5	250.0	1.29E-05	2.6
9	1037.5	452.5	0.0	1.10E-05	3.0
10	75.0	452.5	125.0	2.30E-06	51.3
11	1609.8	718.6	199.3	8.08E-06	0.2
12	1037.5	5.0	125.0	2.73E-05	9.9
13	1037.5	452.5	125.0	1.26E-05	2.2
14	2000.0	452.5	125.0	1.86E-05	3.2
15	1609.8	718.6	50.7	1.42E-05	17.5
16	465.2	186.4	50.7	1.70E-05	1.9
17	465.2	718.6	199.3	2.10E-06	15.7
18	465.2	186.4	199.3	1.93E-05	4.5
19	1037.5	452.5	125.0	1.18E-05	7.1
20	1037.5	452.5	125.0	1.36E-05	2.4

Table 1.10: Estimates and hypothesis tests for the parameters of the quadratic model fitted to the log transformed data for the concentration of the Fe^{2+}-$(Ferrozine)_3$ complex formed.

Parameter	βx key	Coefficient estimate	Standard Error	F Value	p-value-Prob > F	% impact
β0	intercept	12.43	0.590			
β1	Ferrozine	4.08	0.392	108.66	1.08E-06	25.44
β2	PO_4^{3-}	-6.51	0.392	275.97	1.31E-08	64.61
β3	Fe^{3+}	0.016	0.392	0.0017	0.97	4E-4
β12	Fz-[PO_4^{3-}]	0.87	0.512	3.00	0.11	0.70
β13	Fz-Fe^{3+}	-0.84	0.512	2.69	0.13	0.63
β23	[PO_4^{3-}]-Fe^{3+}	-1.28	0.512	6.25	0.031	1.46
β11	$[Fz]^2$	-0.62	0.381	2.66	0.13	0.62
β22	$[PO_4^{3-}]^2$	1.93	0.381	25.61	4.9E-4	6.00
β33	$[Fe3+]^2$	-0.11	0.381	8.0E-2	0.78	0.019

Table 1.11: ANOVA for the response surface generated by the quadratic model fitted to the log transformed data for Fe-(Ferrozine)$_3$ complex formation.

Source	Squares	df	Square	Value	Prob > F	
Model	894.7972	9	47.4615	47.4615	5E-07	significant
Residual	20.94791	10	2.094791			
Lack of Fit	17.40935	5	3.48187	4.919896	0.052568	not significant
Pure Error	3.53856	5	0.707712			
Cor Total	915.7452	19				
Std. Dev.	1.447339		R-Squared	0.977125		
Mean	13.24812		Adj R-Squared	0.956537		
C.V. %	10.92486		Pred R-Squared	0.845168		
PRESS	141.7871		Adeq Precision	26.47896		

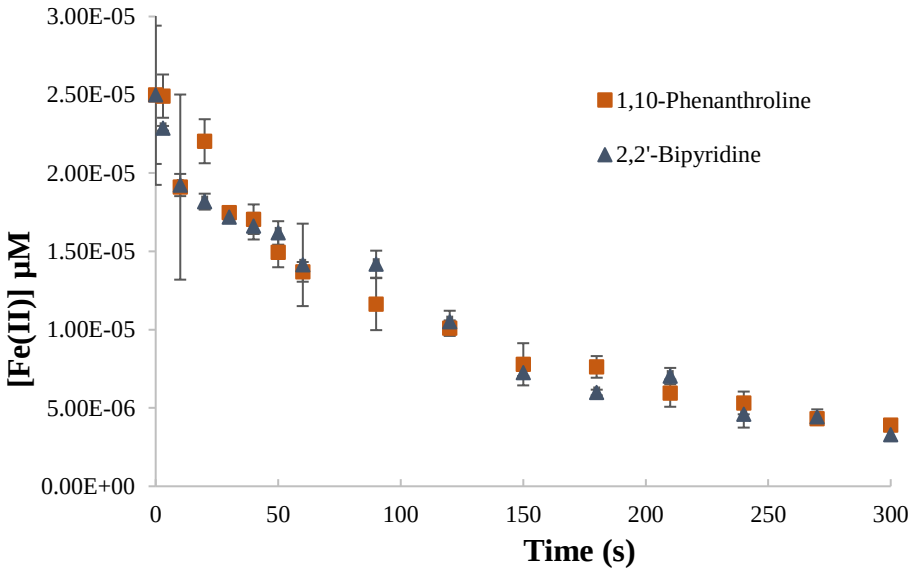

Figure 1.1: Oxidation of Fe^{2+} in oxygen saturated solutions. Conditions: 25 mM HEPES buffer (pH 7.8).

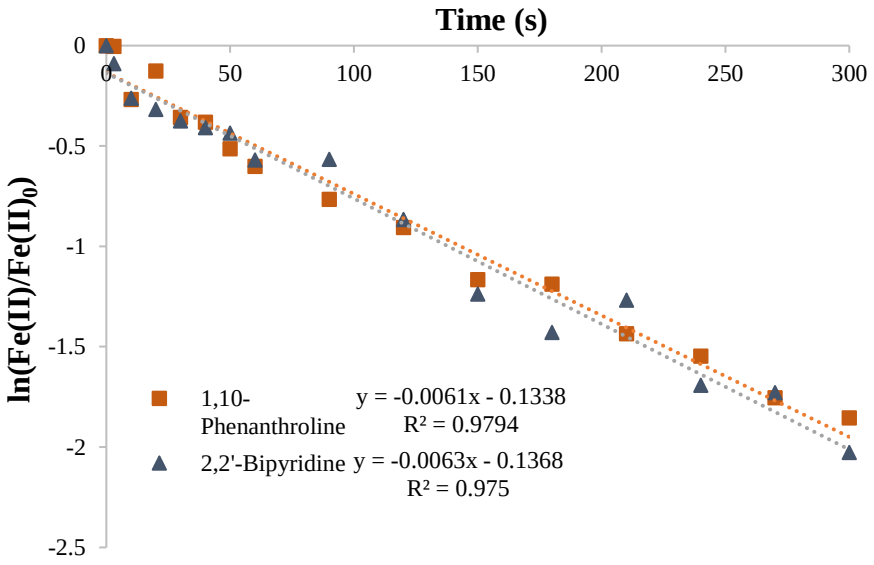

Figure 1.2: First order oxidation of Fe^{2+} in oxygen saturated solutions. Conditions: 25 mM HEPES buffer (pH 7.8).

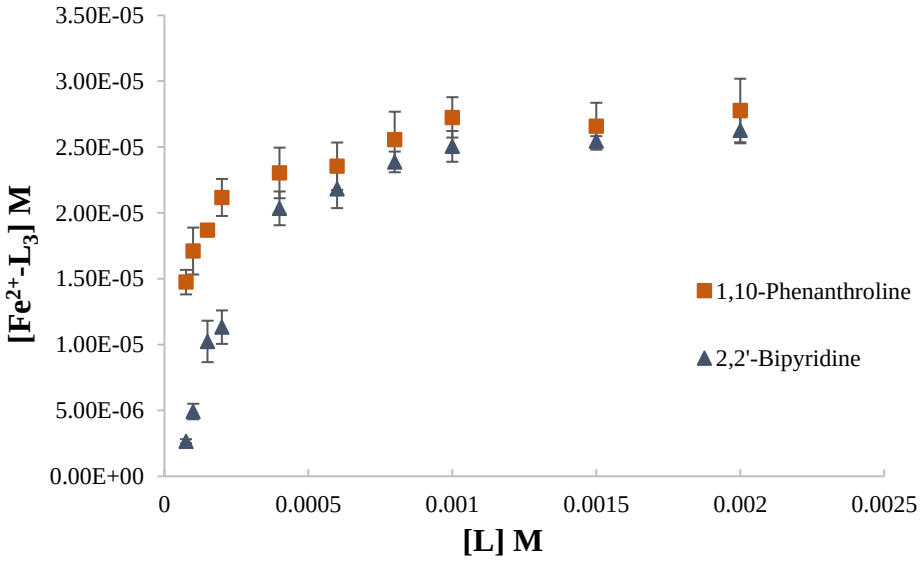

Figure 1.3: Variation in the [Fe^{2+}-ligand] complex formed with varying ligand concentration. Conditions: $[phosphate]_{total}$ = 100 mM (pH 7.8).

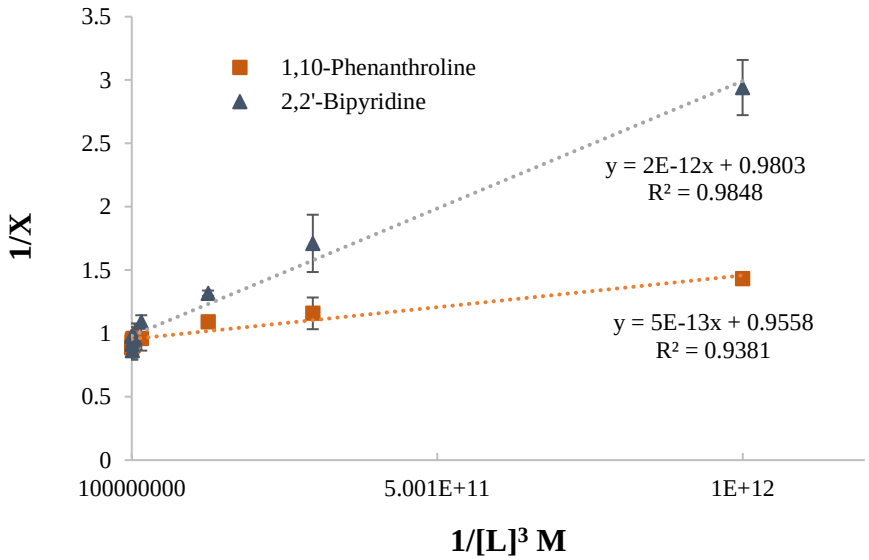

Figure 1.4: A representative plot showing the linear correlation of the colorimetric data for varying ligand concentrations. Conditions; $[phosphate]_{total}$ = 25 mM (pH 7.8). X= fraction of Fe^{2+} reacting with the ligand (L).

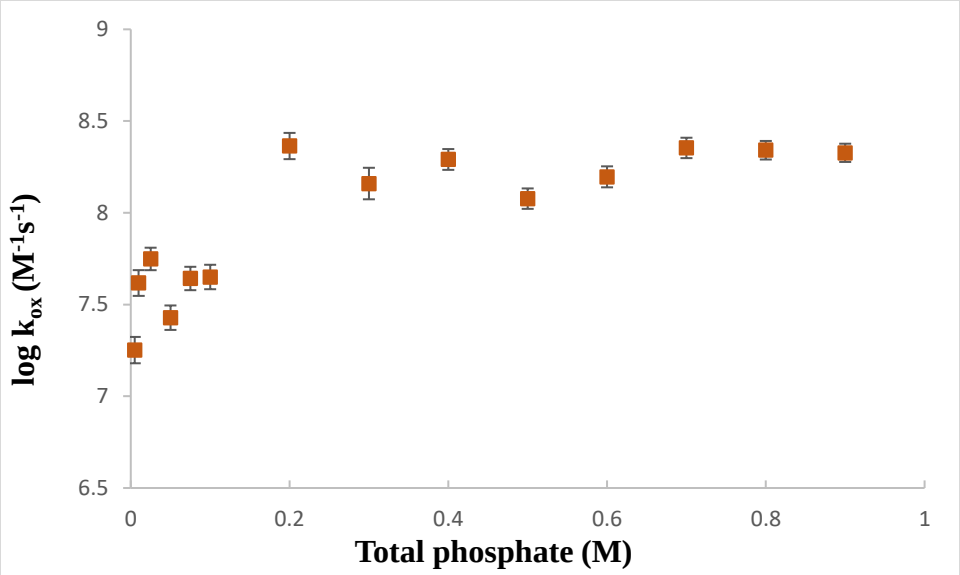

Figure 1.5: Variation in log k_{ox} vs total phopshate calculated using the Fe^{2+} complexation with 1,10-Phenanthroline (pH 7.8)

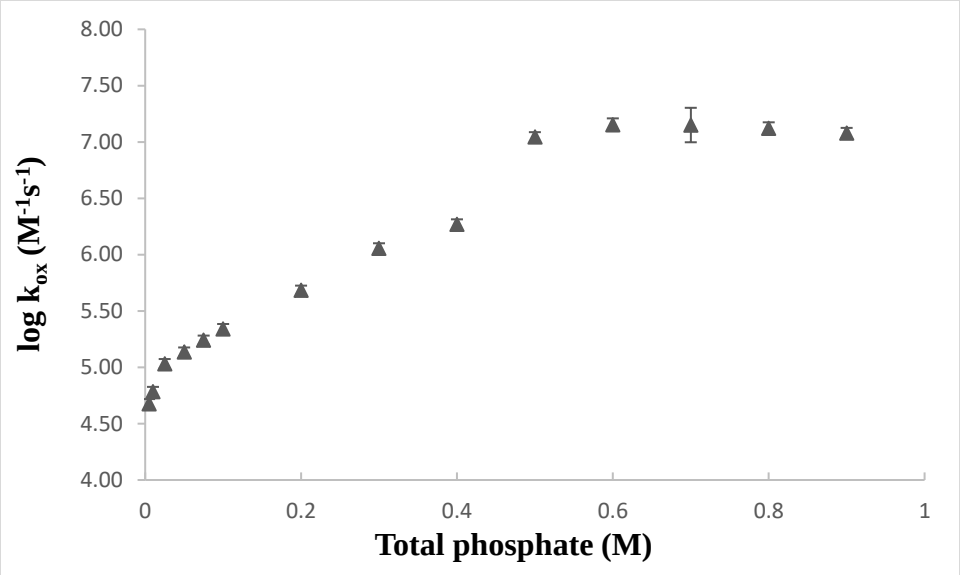

Figure 1.6: Variation in log k_{ox} vs total phosphate calculated using the Fe^{2+} complexation with 2,2'-Biyridine (pH 7.8)

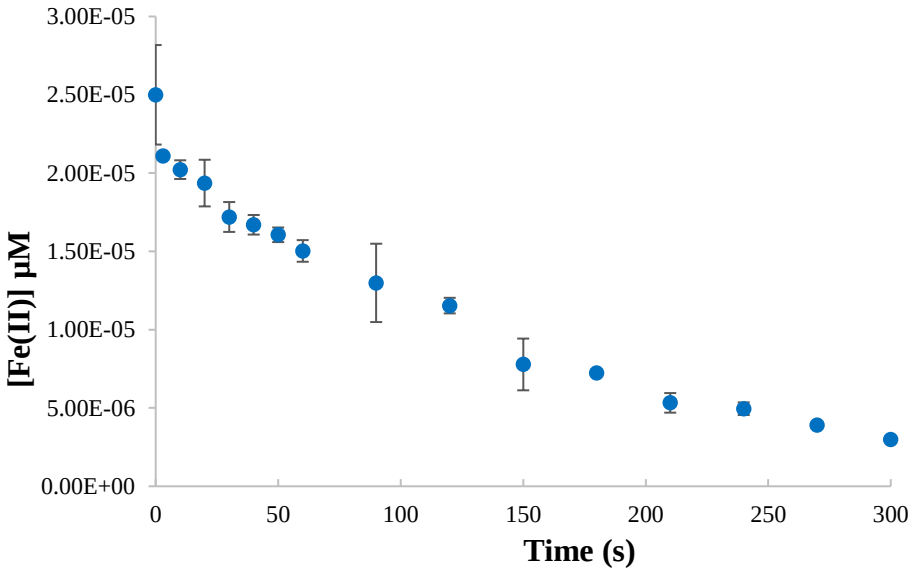

Figure 1.7: Oxidation of Fe^{2+} in oxygen saturated solutions measured using ferrozine. Conditions: 25 mM HEPES buffer (pH 7.8).

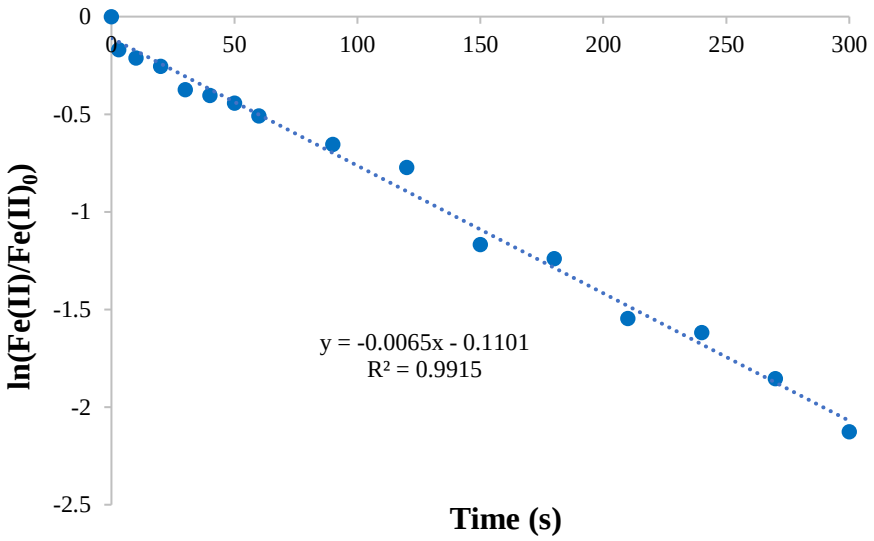

Figure 1.8: First order oxidation of Fe^{2+} in oxygen saturated solutions measured using ferrozine. Conditions: 25 mM HEPES buffer (pH 7.8).

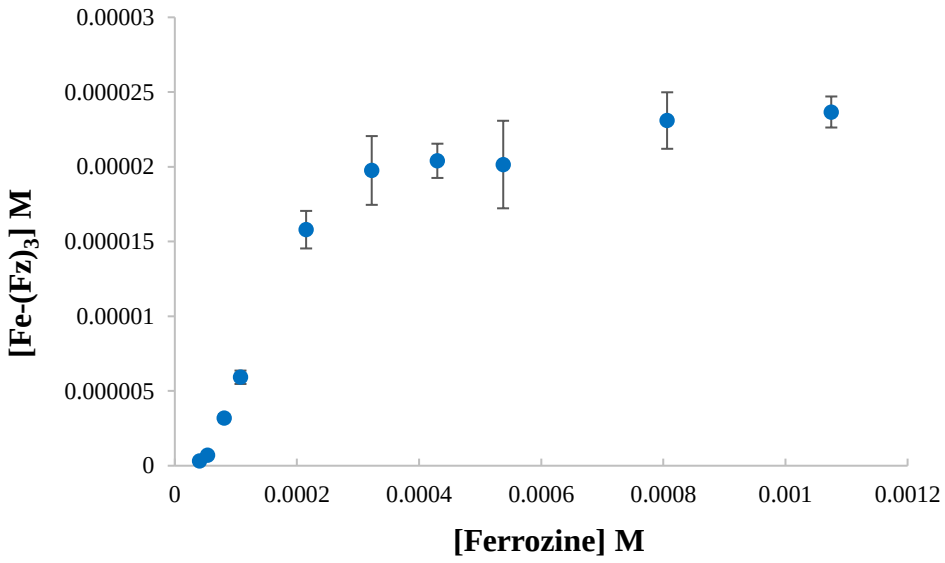

Figure 1.9: Variation in the [Fe^{2+}-ferrozine$_3$] complex formed with varying ligand concentration. Conditions: [phosphate]$_{total}$ = 100 mM (pH 7.8).

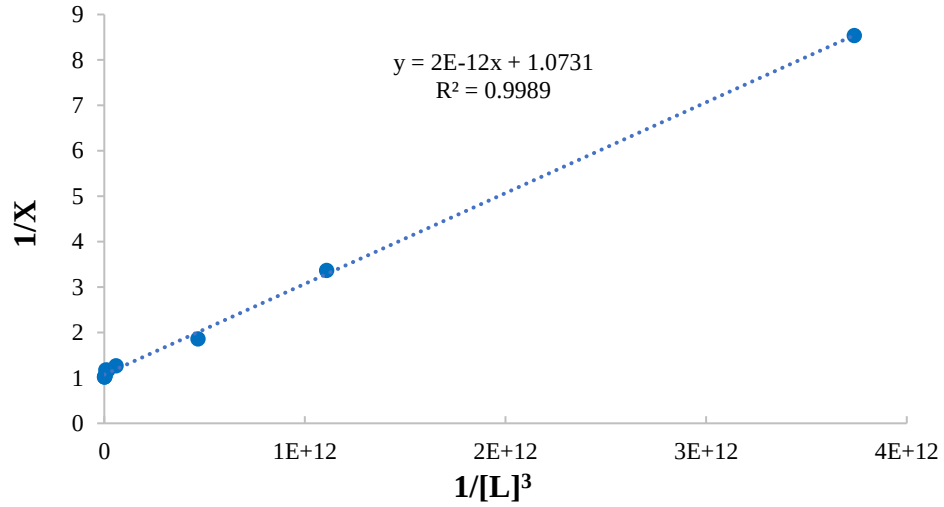

Figure 1.10: A representative plot showing the linear correlation of the colorimetric data for varying ligand (ferrozine) concentrations. Conditions; $[phosphate]_{total}$ = 5 mM (pH 7.8). X= fraction of Fe^{2+} reacting with the ligand (L).

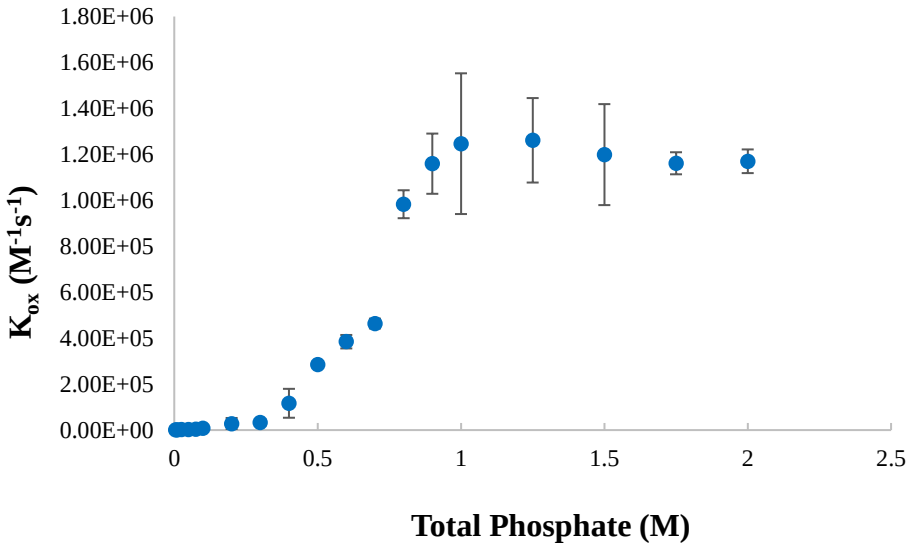

Figure 1.11: Variation in k_{ox} vs total phosphate calculated using the Fe^{2+} complexation with ferrozine (pH 7.8).

CHAPTER 2

ASSESSMENT OF THE MAGNITUDE OF SHALLOW SEAWATER-POREWATER EXCHANGE IN SALT MARSH SYSTEMS

2.1 Abstract

Salt marshes are among key habitats in estuarine ecosystems marked with high capacity for processing particulate phases, high productivity and can be important sinks for carbon burial. Salt marsh sediments are thought to have low permeability, however, advective flow mediated by plant roots and animal burrows contributes to seawater-porewater exchange. Circulation of water through shallow sediment can deliver oxygen to the typically anoxic sediment and promote oxygen mediated transformation of organic carbon and other reactive elements. Here we present the use of Ra as a tracer to assess the net advective flux through sediment as an integration of different contributors in a South Carolina salt marsh system. Sediment cores were collected during four field campaigns from contrasting locations in the marsh to evaluate the spatial variabilities between cores. In conjunction with the core collections, ^{224}Ra activity in porewater and the water column during tidal cycles were also measured. The calculated fluxes varied depending on the physical characteristics of the cores with higher flow rates reported in cores collected at sites with high grass and burrow density. The high fluxes support coastal marsh systems' ability to act as both reactors and reservoirs for particulate and dissolved organic carbon as they transit between terrestrial and marine systems.

2.2 Introduction

Estuarine systems are transition zones between terrestrial/riverine systems and the oceans that play a vital role in processing organic carbon. Their capacity to act as global carbon sinks have been widely documented.[53-61] Many studies also propose the possibility of estuarine waters being sources of CO_2 to the atmosphere, significant enough to nearly

counterbalance the CO_2 sink in continental- shelves.[56-62,63] This would suggest that most of the terrestrially driven organic carbon undergoes microbial respiration during the transit from land to ocean. However, decomposition studies have shown only 10-50% of riverine organic carbon is processed in estuaries.[56,64-66] Following this discrepancy, it has been suggested that the CO_2 loss from estuaries largely represent the microbial decomposition of organic carbon produced in coastal marsh systems whereas most riverine carbon bypasses the estuarine zone due to their short transit times.[67-69] This has highlighted the importance of differentiating between estuarine systems that receive substantial river discharge and those that receive minimal freshwater inputs when estimating carbon fluxes and budgets in coastal zones.[69-71]

The exchange and decomposition of organic rich phases and low carbon burial is predicted in permeable marine sands due to the advective supply of oxygenated water.[72-74] In contrast, salt marsh sediments are fine-grained and thought to be oxygen limited resulting in high particulate trapping and high carbon burial.[75-76] This assumed low permeability is thought to limit the exchange of pore waters with surface waters and the transformation of particulate species in these muddy marsh systems. However, recent studies suggest that the advective flow in these systems may have been underestimated in their ability to transform terrestrial carbon and nutrients at the land-ocean interface.[76]

Despite the low permeability, tracer studies indicate the water exchange in saltmarsh systems are higher than expected.[77] Studies predict high hydraulic conductivities that do not directly correlate with the sediment permeability in saltmarsh systems.[77,78] Studies of nutrient supply to marsh grasses suggest that the grasses contribute to particle settling and their root system can facilitate advective flow. Vertical and horizontal

advective flow in the subsurface sediments around the root zone supports water and nutrient circulation at higher rates than would be predicted based on sediment permeability alone.[79-81] These results suggest that other factors such as advective flow may also play a significant role in predicting the hydraulic conductivity in shallow marsh sediment.

The ability of vegetated marsh systems to preferentially trap particulate phases indicates the potential value of these systems as bioreactors, as has been proposed for more permeable sediment systems.[72,73] Variations in the grass canopy morphologies influence flow dynamics, particle advection and settling. Several studies have documented the reduction of water velocity and the subsequent promotion of particle retention by grass canopies of several *Spartina* species in coastal marsh systems.[82-86] In addition to plants, burrowing activities of benthic macrofaunal organisms can enhance solute exchange fluxes across sediment-water interface where burrows act as passive sediment traps.[87-90] The trapping of organic matter by marsh grass canopies and benthic burrowing activities can have a critical impact on the carbon and nutrient mass balance in salt marsh systems.[91,92] Thus, factors that affect the available oxidants and the associated rate of regeneration of particle phases play a critical role in the net burial of particle associated phases. Organic particles get deposited on the oxic sediment surface first undergo aerobic degradation and are subsequently buried in anoxic layers where anaerobic degradation takes place. Due to the less labile nature of partially degraded organic matter buried in anoxic sediment, anaerobic decomposition is relatively slower.[93-95] Thus, the nature of the organic material plays a role in deciding whether aerobic or anaerobic pathways have the larger impact on the decomposition of organic matter in a system. Recalcitrant organic matter can resist anaerobic degradation, enhancing the carbon preservation in systems with higher amounts

of refractory carbon. High vertical transport rates can also increase the deposition flux reducing the aerobic decomposition in the upper layers. Overall, the relationships between flow, particle deposition and carbon turnover support a system adapted for nutrient recycling which suggest the potential significance of advective exchange of electron acceptors that drive particle transformation.[91,96-98]

Radium isotopes are widely used as tracers for investigating oceanographic processes and chemical fluxes to the ocean.[77,99-104] The four isotopes of Ra; ^{224}Ra, ^{223}Ra, ^{228}Ra and ^{226}Ra have half-lives ranging from 3.6 days to 1600 years. These broad variations in half-lives make Ra isotopes excellent tracers to study processes that take place over multiple spatial and temporal scales. The short-lived ^{223}Ra and ^{224}Ra (half-lives of 11.4 and 3.66 days respectively) are useful in studying processes on time scales of several days to weeks. [100,105-110]

Based on the delayed coincidence counting system developed by Moore and Arnold,[111] Cai *et.al.* developed an approach for using the ^{228}Th/^{224}Ra disequilibrium as an indicator of advective water movement in river sediment.[112-115] The method uses the relatively higher mobility of ^{224}Ra in pore water compared to the ^{228}Th parent to estimate the loss of the daughter due to pore water exchange. In seawater, ^{224}Ra is produced via the alpha decay of its parent, ^{228}Th. ^{228}Th is highly particle reactive and has strong affinity to remain bound to sediment particulate phases. In contrast, the ^{224}Ra daughter has drastically different geochemical characteristics dependent on the ionic strength. While it is strongly particle bound in freshwater, as the concentration of other alkaline earth elements Ca^{2+} and Mg^{2+} increases down the estuary, ^{224}Ra is desorbed from the particle surface. Therefore, if seawater or brackish water flows through sediment, ^{224}Ra can be mobilized and migrate

across the sediment-water interface to overlying water creating a disequilibrium between ^{224}Ra and ^{228}Th.

In this chapter, water column and pore water ^{224}Ra activity as well as $^{224}Ra/^{228}Th$ sediment disequilibrium measured from different sites in the Folly Beach marsh system to verify that surface marsh sediments are subject to advective flow are presented. Further, the magnitude of that flow was measured as a function of vegetation and burrow density. The overall goal of this work was to test the applicability of the disequilibrium between sediment bound ^{228}Th and its daughter ^{224}Ra to obtain an integrated result of the multiple factors that contribute to the advective flow in the marsh system. Two sampling campaigns were arranged before and aftermath of Hurricane Irma to investigate the impact of the storm on the hydrodynamics of the marsh system.

2.3 Experimental Methods

Sampling Sites

The sediment core samples and water samples were collected at different sites in the Folly creek watershed in Folly Beach, South Carolina during five field campaigns in 2017 (March, May, July and September). The locations were selected to minimize contributions from rivers and groundwater inputs, except for the near surface circulation through permeable marsh sediment. Permeable layers of sand and/or shell hash present at the sites can support rapid horizontal flow of water in and out of the upper 50 cm of the marsh sediment near the creek edge. The saline water inputs to the Folly Creek watershed are provided by the Folly River, Folly Creek, the intercoastal waterway and other branching creeks with minimal freshwater inputs except for local precipitation. The site locations were selected

specifically to minimize contributions to the system from rivers or groundwater inputs other than the near surface circulation through permeable marsh sediment. The watershed shares an inlet with the Stono River watershed, a tidal channel in Southeast South Carolina. The main land formation is the barrier island of Folly Beach, on the southeastern side of the watershed.

Site A is a marsh edge location with a dock and a floating platform providing marsh and creek access while site B is a low energy site in the center of the marsh (Figure 2.1). Sampling in September coincided with a major storm event; hurricane Irma, which made landfall on the US East coast on September 10th, 2017 resulting in heavy rainfall and a surge in wave action in the sampling area. Sampling sessions were carried out before and after the hurricane (September 7th and 14th) to assess the impact of the storm on the hydraulic dynamics of the salt marsh system.

Pore Water and Creek Water Collection and Analysis

Creek water samples were collected from site A at different time points of a tidal cycle during trips in May and September. During the May campaign two additional samples were collected at Folly River Boat Ramp approximately 2 miles from site A and a seawater sample near the Folly Beach Pier. Two water samples, at low and high tides were collected in July. The samples were collected to 20 L carboys and filtered through columns containing acrylic fiber coated with MnO_2 (Mn fibers). The MnO_2 serves to adsorb the dissolved Ra in the water samples. Low tide samples with high particulate loads were set aside for particles to settle before filtration. Upon bringing the samples to the laboratory, the columns containing the Mn fibers were rinsed, partially air dried to remove excess water until no further droplets of water emerged out of the bottom of the column. Subsequently, the activities of ^{223}Ra and ^{224}Ra were measured using a delayed coincidence

counting system (RaDeCC).[111, 115,116] This system monitors the alpha decays of the short-lived Rn daughters of ^{223}Ra and ^{224}Ra. Samples were counted within 18 hours to minimize counting errors; typical yields were 800-1000 counts for ^{220}Rn (the daughter of ^{224}Ra). After the initial counting, the Mn fiber samples were aged for 3-4 weeks and measured again to determine ^{228}Th and correct for ^{224}Ra. Before counting, the weight of the Mn fiber samples were adjusted to match the weights of the first counting by adding water. Pore water samples collected on a falling tide and were coincident with the sediment core sampling points during May and September trips. The processing and analysis were similar to the creek water samples.

Sediment Core Collection and Analysis

Two sediment core samples from sites A and B were collected during the March trip. In May, two samples were collected from two separate locations at site A. The first sampling point was located on the marsh edge off the dock while the second point was more towards the center of the marsh approximately 30 m from the first sampling point. Both locations were populated with *Spartina alterniflora* grass. Both cores from September 7th trip were from the marsh edge location at site A one was collected from a spot previously sampled and contained recently deposited sediment (and no plant roots or obvious burrows) the second core was collected within 10-20 cm adjacent to living marsh grass. The first core location for September 14th was the near those collected in May and September 7th. This was treated as a reference sample for comparing pre-and post-hurricane data. The second location was approximately 20 m from the first location, adjacent to a small creek with no marsh grass visible in the surrounding area. The sampling site following the hurricane had lost a great deal of the grass canopy and was covered with a thick mat (as

much as a half meter) of marsh grass that had been uprooted and later deposited by the storm.

The cores were within 25-30 cm in length and processed immediately after bringing to the laboratory. The cores were processed similar to the method developed by Cai. *et.al.*[112] Each core was cut into 4-5 cm sections, transferred to a Teflon beaker. To each of the sediment section, 150 mL of 18MΩ water was added to form a slurry. This was sonicated to 15-20 minutes. The pH of the slurry was adjusted to pH 9 by dropwise addition of NH_4OH. Afterwards, 1.0 mL of $KMnO_4$ (3.0 gL^{-1}) and 1.0 mL of $MnCl_2$ (8.0 g $MnCl_2.4H_2O$ L^{-1}) were added to form a suspension of MnO_2. Subsequently, the slurry was filtered onto a 142 mm GF/F filter. This was then transferred into a modified sample chamber and counted for ^{224}Ra activities using RaDeCC. Similar to the water samples, the sediment samples were aged for 3-4 weeks, weights adjusted and measured again to determine ^{228}Th and correct for ^{224}Ra. The relative errors of final ^{224}Ra activities were less than 10%. Within the counting period, the number of counts for ^{223}Ra was very low, resulting in higher errors associated with ^{223}Ra activities (~ 25%). Due to this high uncertainty, the flow rate estimations in this study were based only on ^{224}Ra activities.

2.4 Results

The ^{224}Ra concentrations in water samples collected from site A in May showed significant variation within the tidal cycle. At low tide, the ^{224}Ra concentration was 7.6(±0.3) dpm/L. With rising tide, the concentrations fell to 2.3 – 3.0 dpm/L and reached 1.9(±0.1) dpm/L at high tide. As the tide fell, the concentration remained fairly low at 1.8(±0.1) dpm/L to finally increase to 8.0(±0.4) dpm/L at next low tide (Figure 2.2). The two water samples from the boat ramp at rising and falling tide were 1.7(±0.3) and

0.3(±0.01) dpm/L respectively. The concentration of the seawater sample collected near the Folly Beach Pier at rising tide was 0.5(±0.02) dpm/L. Pore water from site A had a ^{224}Ra concentration of 10.4(±0.4) dpm/L. The high tide and low tide water samples from Site A in July had 224Ra levels of 1.8(±0.1) and 5.5(±0.1) dpm/L respectively. The samples collected during the September 7th trip recorded ^{224}Ra concentrations of 5.6(±0.2) and 6.9(±0.2) dpm/L for the low tide and pore water samples respectively. The ^{224}Ra concentrations water samples collected during a tidal cycle in September 14th trip followed a trend similar to the samples collected in May. During falling tide, the concentration was 1.5(±0.1) dpm/L and increased to 4.7(±0.2) at low tide. As the tide rose the concentration fell back to 2.0(±0.1) dpm/L and further decreased to 1.7(±0.1) at high tide (Figure 2.2). Salinities recorded for the water samples during the tidal cycle ranged between 26.8 – 28.7 ppt, observed at low and high tides respectively. The pore water ^{224}Ra activity collected from the reference core sampling point was 6.7(±0.2) dpm/L. The salinity was 27.6 ppt. At the second core site (non-vegetated), the pore water ^{224}Ra activity was 8.5(±0.2) dpm/L and the salinity was also relatively higher at 29.7 ppt.

Sediment ^{228}Th activities for all cores at all depth intervals varied between 0.80(±0.03) – 0.39(±0.02) dpm/g, except for the 1-4 cm interval for marsh edge core collected in March, which had an activity of 1.06(±0.03) dpm/g. Generally, the higher activities were observed in the upper sediment (0-5 cm depth), with activities decreasing with depth. However, this trend was not consistent throughout the cores, as several showed erratic variations in ^{228}Th activities in the middle portion (5-20 cm depth) of the cores.

The net pore water exchange, as export of ^{224}Ra activity in upper sediment, was estimated by integrating the difference between the activity of ^{224}Ra at the time of sample

collection and the activity of ^{224}Ra once the sample was allowed to come to secular equilibrium with the surface bound parent, ^{228}Th. In this case the disequilibrium was determined over the upper 0-25 cm of the sediment column. The sediment-bound ^{224}Ra and ^{228}Th inventories in the upper 25 cm of the sediment column were considered to be at steady state with respect to particulate inputs or losses on the timescale of several ^{224}Ra half-lives ($t_{1/2}$ = 3.6 days). Thus, within the uncertainty of the measurements, disequilibrium reflects the exchange of the pore water inventory of ^{224}Ra. The steady-state assumption allows the calculation of the loss of ^{224}Ra activity due to export as Eq. (2.1) below (after Cai *et al.* 2014).[113]

The rate of ^{224}Ra export (as activity) was estimated by:

$$F_{Ra} = \lambda_{224Ra}(A_{228Th}-A_{224Ra}) \quad \text{Eq 2.1}$$

Where F_{Ra} is the loss of sediment ^{224}Ra activity, in excess of decay, expressed as pore water ^{224}Ra export in disintegrations per minute (dpm) of ^{224}Ra cm^{-2} day^{-1}. λ_{224Ra} is the decay constant for ^{224}Ra (0.189 day^{-1}), and A_{228Th} and A_{224Ra} are the activities of ^{228}Th and ^{224}Ra in units of dpm per gram of sediment.

The export of ^{224}Ra activity (F_{Ra}) as pore water flux was estimated using pore water ^{224}Ra activities calculated for the pore water samples collected on each sampling trip (Table 2.1). These calculations yielded a pore water exchange rate of 118(±1) Lm^{-2}day^{-1} for the core from site A in March (Figure 2.3). For the site B core, the exchange rate was 102(±1) Lm^{-2}day^{-1}. A burrow was present between 10-15 cm depth of this core, which is reflected by the significant deficit observed in that depth range (Figure 2.4). The marsh edge core from May yielded a pore water exchange rate of 125(±10) Lm^{-2}day^{-1} (Figure 2.5). Similarly, the core collected towards the center of the marsh resulted in 147(±12) Lm^{-2}day^{-}

[1] (Figure 2.6). A significant difference was observed between the pore water exchange rates for the two cores collected during the September 7th trip before hurricane Irma made landfall. The two cores yielded exchange rates of 69(±17) and 128(±16) $Lm^{-2}day^{-1}$ (Figures 2.7 and 2.8). Here, the sediment core with the lower exchange rate was sampled from a previous sampling point that has refilled since the earlier collection. This was specifically chosen to evaluate the advection without any root or burrow influence. The higher exchange rate resulted from a core obtained from the rhizosphere of the vegetated portion of the marsh edge that has not disturbed during previous sampling. The reference core from the post hurricane trip on September 14th, again from the rhizosphere but not disturbed during previous sampling, yielded a pore water exchange rate of 86(±20) $Lm^{-2}day^{-1}$ (Figure 2.9). The second core collected in a section of un-vegetated marsh edge had a similar exchange rate of 74(±17) $Lm^{-2}day^{-1}$. This core collected near a creek had a high-water content and a burrow was present within 10-20 cm of the core, which affected the observed disequilibrium at both 12.5 cm and 17.5 cm sample intervals (Figure 2.10).

2.5 Discussion

During the two tidal cycles, the highest creek water ^{224}Ra activities were measured for low tide water samples. In sediments, ^{224}Ra is continuously produced by its insoluble ^{228}Th parent. As saline water circulates through sediment, Ra bound to sediment surfaces readily undergo desorption, increasing the ^{224}Ra concentration in exchanging water and is observed as enrichment in the creek water. During low tide, the circulating seawater is drawn out of the marsh sediment. The resultant compression of the marsh sediment during low tide could be observed as the extensive cracking that appeared on the sediment surface. Similarly, as saline water flush through the marsh sediment, ^{224}Ra is mixed into the water

flux leading to elevated ^{224}Ra activities in pore water. This was observed in the dissimilar ^{224}Ra activities of the porewater samples from September 14. The high salinity porewater sample had a higher ^{224}Ra activity compared to the low salinity sample. This is consistent with the desorption of Ra from particle phases as saline water is flushed through the marsh sediment increasing the porewater ^{224}Ra level. Since the riverine freshwater inputs to the sampling sites are minimal, the Ra sources include Ra released from the marsh sediment and that advected into the salt marsh system by groundwater. The difference between the ^{224}Ra activity in the open seawater sample collected at the pier and the low tide water samples represent the Ra input into the water column from circulation through sediments in landward sections of the marsh.

Comparatively higher ^{228}Th activities observed in surface sediment are consistent with ^{228}Th being supplied via scavenging in the overlying water column by suspended particles that subsequently settle on the surface. The ^{224}Ra deficit observed throughout the lengths of the cores suggest that advective flow of water is supported in the upper ~30cm of shallow marsh sediment.

The pore water exchange rates for the cores collected in March were similar at both sites. The presence of a burrow in the second core facilitated higher water flow as evident by the higher ^{228}Th/^{224}Ra disequilibrium observed in the corresponding depth interval.

The two sampling locations in late Spring (May) were densely populated with cordgrass (*Spartina alterniflora*) and recorded the highest observed flux through the marsh sediment. The calculated advective flows in these cores were potentially impacted by the presence of cordgrass canopies. One possible mechanism for this higher than expected advective flow maybe associated with the compressibility of the sediments due to changes

in cordgrass root volume. A study by Sundby on a similar marsh grass system reported that during summer the root biomass comprises around 25% of the dry weight of the total mass up to 20 cm depth.[117] Sediment volume typically increases with the additions of root and rhizome tissues. Grass roots contain intercellular gas filled spaces that can account up to 60% of the total root volume. During tidal inundation, the partial pressure of oxygen within the roots have been found to vary within 20-65% in order to facilitate underwater gas exchange.[118, 119] As a result, the compressibility of roots within the marsh sediment can bring about a substantial volume change. Thereby, a greater flow of water can be supported by the sediment surrounding the grass root system. While the root dynamics may not be the sole factor in deciding the advective flow, it can play a significant role in these systems.

The core with the lower porewater exchange, collected in the pre-hurricane trip was from a previous sampling point that had since trapped the eroding sediment. No burrows or roots were observed within the core. The newly deposited sediment appeared to be unaffected by the neighboring grass root network. Thus, this core was considered a low-end estimation for the porewater exchange rate in the marsh system. The observed flux was nearly half that from the second core, sampled from the same location but from an undisturbed point with plenty of cordgrass in the surrounding. This second sample with a 128 $Lm^{-2}day^{-1}$ rate was on par with the grass populated core samples collected in May.

Following Hurricane Irma which made landfall on Florida Keys on September 10th, Charleston, SC received 14 cm of rainfall on September 11th. This is equivalent to about 90% of the average monthly rainfall for the entire month. This also resulted in a wave action reaching up to ~1m in height. In the aftermath, grass was observed to have been uprooted from the marsh system and was piled up along the marsh bank and nearby streets

of the sampling site. Many boardwalks and docks were destroyed and scattered along the marsh. Wave action would have resuspended sediment as well as uprooting marsh grass out. The resultant disruption of the sediment structure, particularly in the rhizosphere may have reduced the volume of root network and burrow structures. This in turn may account for reduction of net exchange between the marsh sediments and surrounding creek water as indicated by lower flow rates measured in the cores collected on September 14th. Water fluxes comparable to those calculated after the hurricane in this study was reported by Dias *et.al.* for a similar location in the Folly marsh system in December.[81] Therefore, this reduction in root mass can be considered to be similar to winter conditions when marsh grass productivity decrease resulting in a decline in root biomass.

The water fluxes calculated in this study are comparable to the groundwater exchange rate of 100 $Lm^{-2}d^{-1}$ reported by Rama and Moore, for the North Inlet salt marsh in South Carolina.[120] Both of these exchange rates calculated in the summer are higher by a factor of 3-4 than the average annual discharge calculated by Krest *et.al.* for the same salt marsh system.[78] Their exchange range of 20-40 $Lm^{-2}d^{-1}$ is more on par with the low-end advection flow estimated in this study and the exchange rates calculated by Dias *et.al.* during the winter.[81]

The large volume flux through muddy marsh sediment is an indication of heightened transport of oxygen to particulate phases and anoxic porewaters rich in reduced species. This sets the stage for a plethora of redox transformations to occur within the upper layers of the marsh sediment. Thereby, these highly productive systems have the potential to support sizable organic carbon degradation which consequently affect the carbon preservation and nutrient flow from salt marsh systems to the coastal oceans.

2.6 Conclusion

$^{228}Th/^{2224}Ra$ disequilibrium technique was used to assess the porewater exchange rate in a South Carolina salt marsh system. Radium deficits were observed throughout the lengths of the cores (~30 cm) collected from various marsh locations implying substantial advective flow that flushes the marsh system with saline water. The fluxes represent the net flow of water through marsh sediment as a collection of different factors that contribute to dissimilar extents. These factors include morphological variations of the sediment including pore spaces and the presence of shell hash layers. Marsh grass and to a lesser extent burrows were seen to facilitate the advection flow. The flow volumes measured after the storm event suggest that the wave action induced by the storm surge has likely changed the sediment morphology hindering the advection pathways associated with grass roots and burrows. These results highlight that despite the low permeability, shallow marsh sediment has the potential to act as both a trap and a bioreactor for particulate and dissolved organic matter prior to the export to continental shelves. Therefore, assessing the flow dynamics of salt marshes which can significantly alter the decomposition patterns in these land-ocean transit zones is pivotal in making estimations of the carbon export from coastal systems and the resultant impact on global nutrient cycles.

Table 2.1: Porewater exchange rates calculated using the sediment core samples

Sampling Month-Year	Location	Porewater Exchange Rate $Lm^{-2}day^{-1}$
March 2017	Site A	118(±1)
March 2017	Site B	102(±1)
May 2017	Site A – marsh edge	125(±10)
May 2017	Site A – towards the center of the marsh	147(±12)
September 2017 pre-hurricane	Site A – previously sampled location	69(±17)
September 2017 pre-hurricane	Site A – undisturbed location	128(±16)
September 2017 post-hurricane	Site A – reference core from marsh edge	86(±20)
September 2017 post-hurricane	Site A – grassless location adjacent to a creek	74(±17)

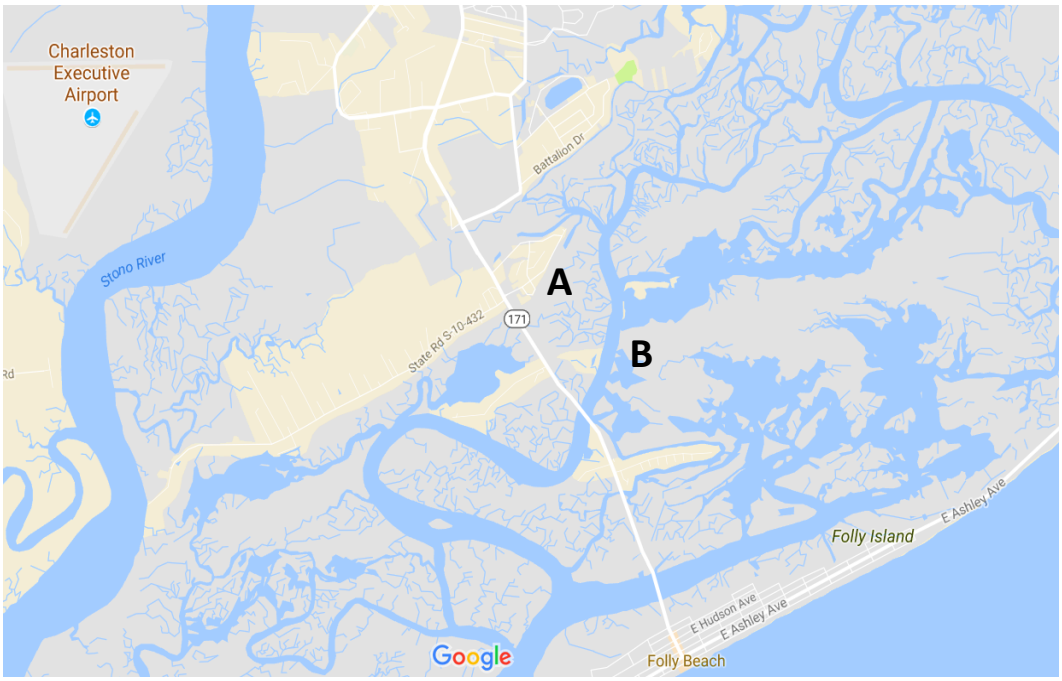

Figure 2.1 The sampling sites in the Folly creek watershed.

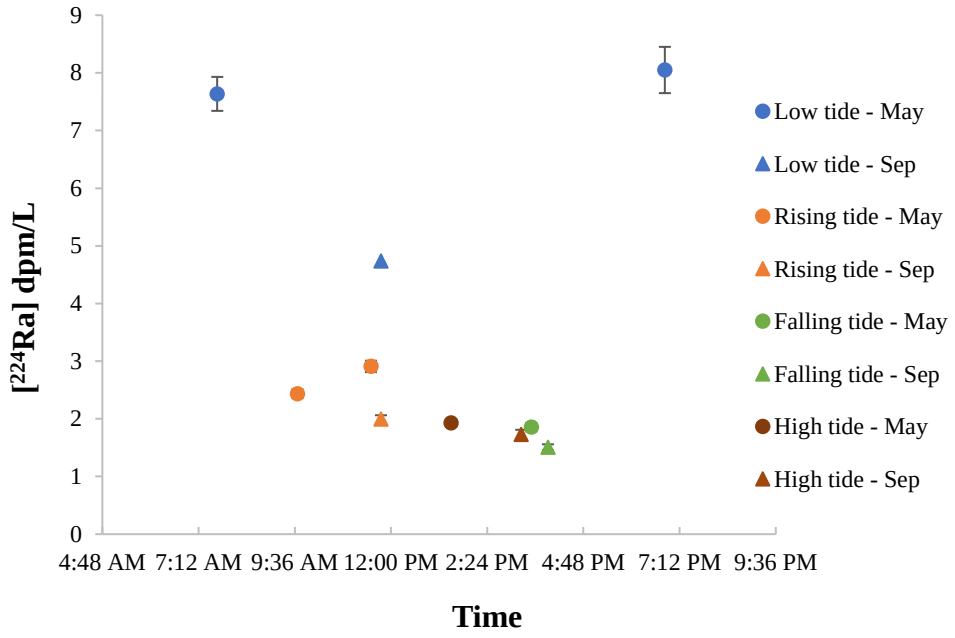

Figure 2.2 Variation in ^{224}Ra concentration in water within a tidal cycle in May and September at site A.

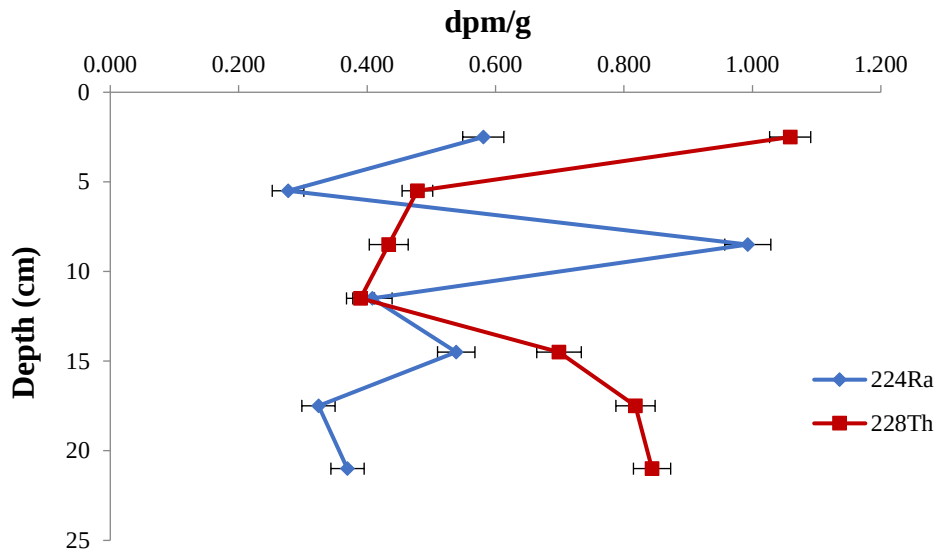

Figure 2.3 $^{224}Ra/^{228}Th$ disequilibrium measured in a sediment core from site A in March.

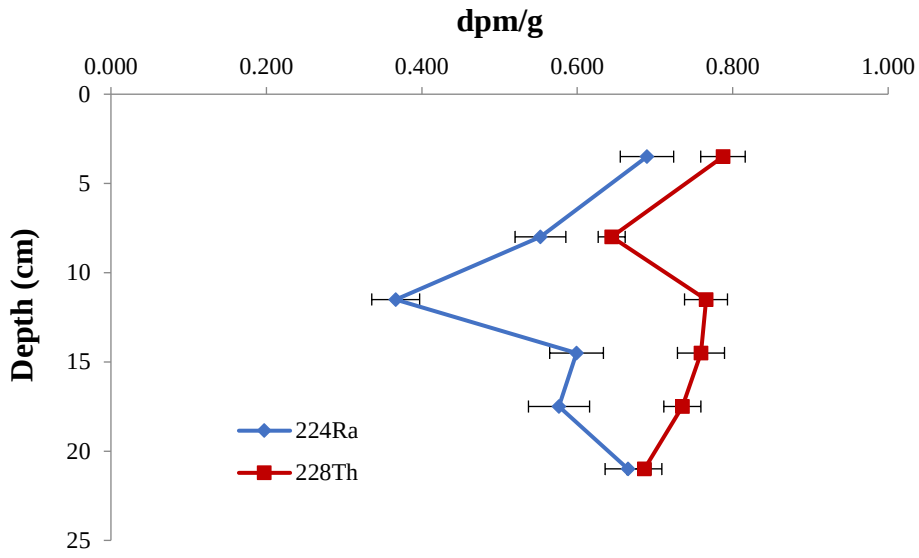

Figure 2.4 $^{224}Ra/^{228}Th$ disequilibrium measured in a sediment core from site B in March.

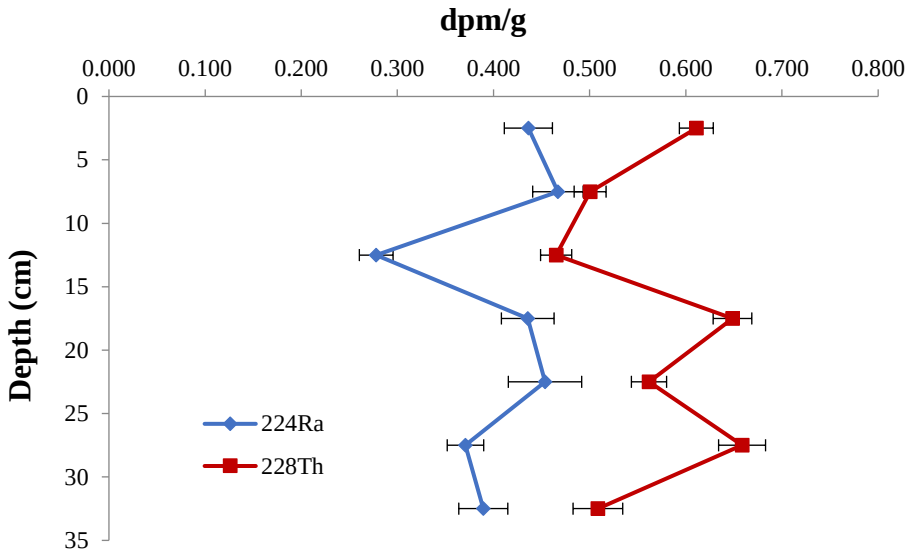

Figure 2.5 $^{224}Ra/^{228}Th$ disequilibrium measured in a sediment core from a marsh edge location at site A in May.

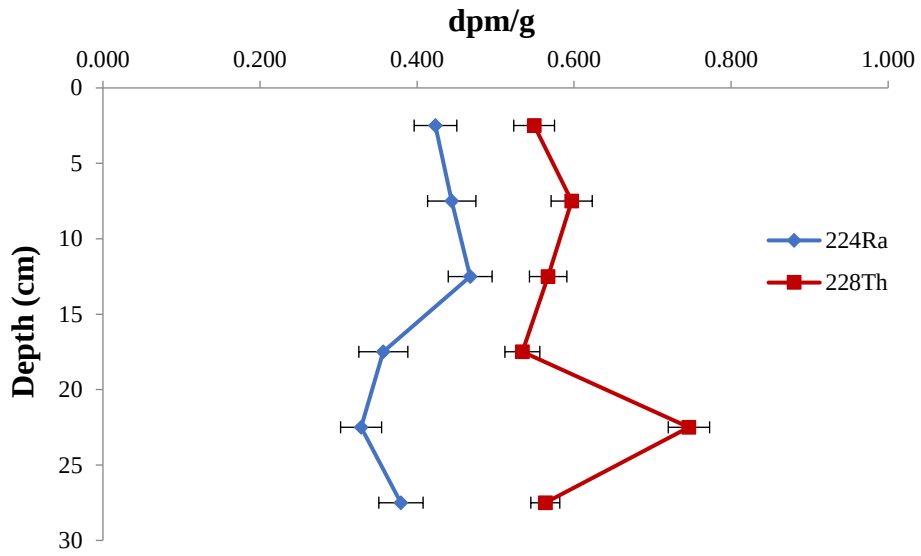

Figure 2.6 $^{224}Ra/^{228}Th$ disequilibrium measured in a sediment core located towards the center of the marsh at site A in May.

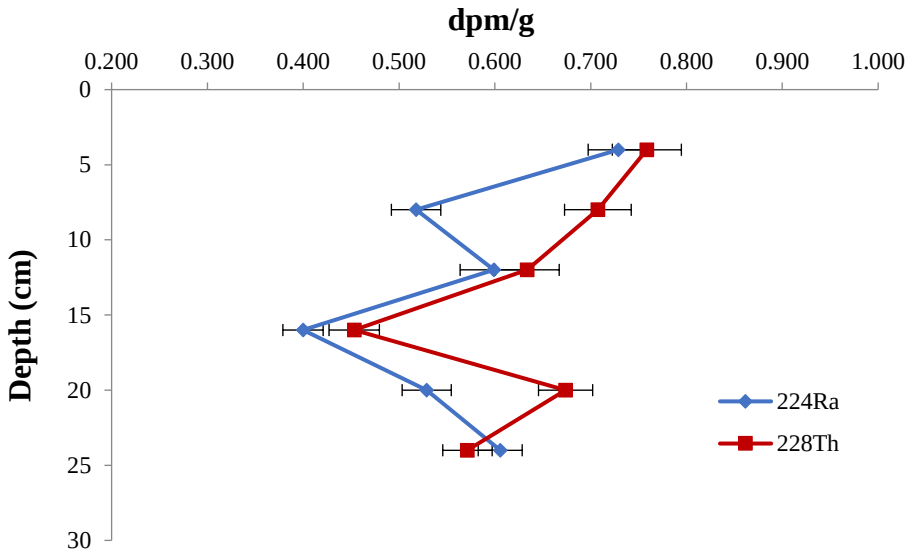

Figure 2.7 $^{224}Ra/^{228}Th$ disequilibrium measured in a sediment core from site A in September (pre-hurricane). The sampling point was a previously sampled point that has been since filled.

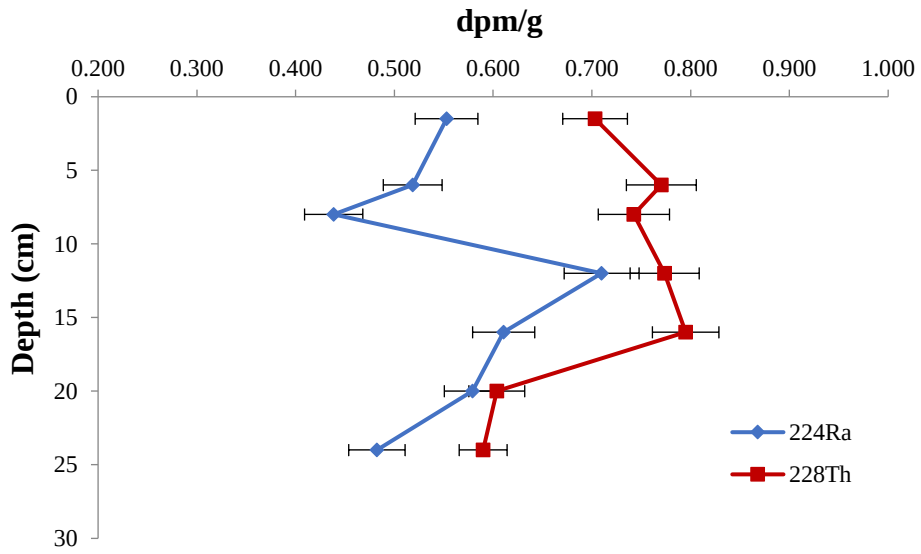

Figure 2.8 $^{224}Ra/^{228}Th$ disequilibrium measured in a sediment core from an undisturbed location at site A in September (pre-hurricane).

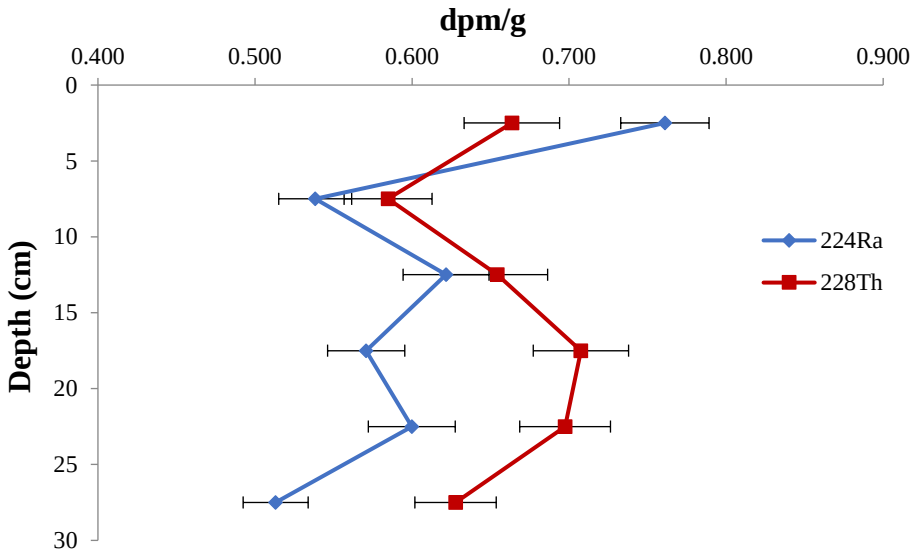

Figure 2.9 $^{224}Ra/^{228}Th$ disequilibrium measured in a sediment core (reference core) from a marsh edge location at site A in September (post-hurricane).

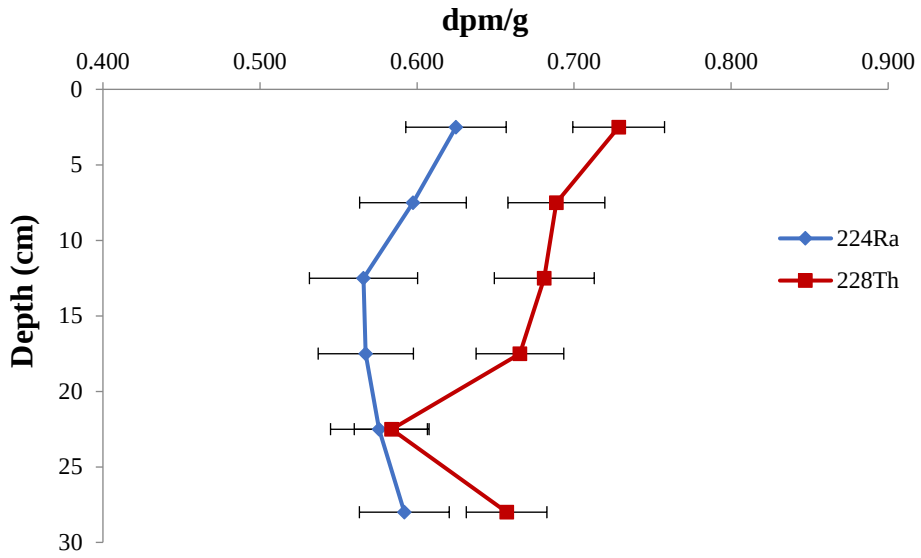

Figure 2.10 $^{224}Ra/^{228}Th$ disequilibrium measured in a sediment core from a grassless location adjacent to a creek at site A in September (post-hurricane).

CHAPTER 3

PRODUCTION OF REACTIVE OXYGEN SPECIES IN THE RHIZOSPHERE OF A *SPARTINA*-DOMINATED SALT MARSH SYSTEM

[81]Dias, D.M.C., Copeland, J.M., Milliken, C.L., Shi, X., Ferry, J.L. and Shaw, T.J. (2016) Production of reactive oxygen species in the rhizophere of a *Spartina*-dominated salt marsh system. *Aquat Geochem.* **22**(5-6), 573-591. Partially reproduced with permission from Springer. Copyright © 2016, Springer.

3.1 Abstract

This chapter reports the presence of a metastable mixture of Fe(II), O_2, superoxide and hydrogen peroxide in sediment pore water in organic carbon-rich sediments in *Spartina alterniflora* dominated salt marsh systems. Field measurements at two different estuarine sites in South Carolina (one heavily urbanized and a protected research reserve) showed a broad region of reactive oxygen species (ROS) production more than 15 cm below the sediment surface within and immediately adjacent to the rhizospheres of *S. alterniflora*. Dissolved Fe(II) was positively correlated with hydrogen peroxide indicating a possible abiotic pathway to ROS production ($r^2 = 0.94$). The null hypothesis was tested that Fe(II) inventories were maintained by protective ligands and thus unreactive with respect to O_2 consumption and ROS production. The addition of an Fe-binding ligand, DTPA, resulted in rapid decline of ROS in pore water, indicating that Fe(II) was labile. The half-life of superoxide under the measured solution conditions was calculated and found to be less than a second. The combination of high lability and persistent ROS was interpreted to indicate a high rate of Fe(II) and O_2 supply to the pore water. The estimated pore water exchange of 54 L m^{-2} day^{-1} was significant but could not support the measured production of ROS alone, the direct exchange of O_2 from the *S. alterniflora* root system may have contributed significantly to the ROS production in the sediments.

3.2 Introduction

Salt marshes and estuaries cover an area of approximately 2.2 x 10^6 km^2 globally[121] and are important regions for both burial and remineralization of organic carbon.[122,123] Marsh and estuarine sediments receive organic carbon from sources that include terrestrial,

marine inputs and autochthonous sources.[124,125] In these systems, the presence of marsh grass can act as a trap for particulate phases often focusing carbon deposition at or near the river or creek edge.[126] Carbon input frequently occurs at higher rates than its microbial oxidation, allowing these systems to act as sinks for organic carbon through physical burial of organic particulates. Carbon burial restricts benthic microbes from easy access to oxygen and the mass flow restriction typically results in the development of shallow redox zones in sediments according to the diagenetic series.[127-131] This physical isolation results in the sedimentary accumulation of materials that are thermodynamically unstable with respect to oxygen but kinetically restricted from reacting with it by mass transport limitations, including Fe(II), Mn(II), and HS^-.[93,96,132,133] The kinetic restrictions are a result of physical isolation and in many cases the spin forbidden nature of some of the molecular processes.[134-137] In sediments having low permeability, concentration gradients for the dissolved products of diagenesis reach a spatial equilibrium based on the relative rates of microbial carbon utilization and diffusion of oxygen into the system from the water column.

The effective permeability of sediments is significantly increased when flora and fauna introduce mechanisms that enable active and passive mixing of oxygen-containing gases or liquids with buried carbon reservoirs. For example, cordgrass *Spartina* species have aerenchyma; spongy vertical structures that enable direct gas transport between aerial portions of the plant and the roots.[119, 138-143] Estuarine fauna may also contribute oxygen to sediments through burrowing activity. Solute transport in marine sediment associated with biogenic irrigation has been well documented. [91,144,145] Conditions that lead to rapid gas exchange between roots and aerial portions of the plant can result in the development of

sharply bounded concentration gradients in redox active species in the sediment around the grass root network.[146-148] This oxygen transport and subsequent radial release coupled with the availability of reduced species in pore water can support the oxidation of redox active species, including the direct oxidation of Fe(II) and the Fe(III) catalyzed oxidation of HS^- and some organic materials. In this manner, the presence of macrofaunal burrows and an extensive grass root system create a three-dimensional network of rapidly oscillating redox gradients in the upper layers of sediment in a salt marsh. This region has the potential to act as a site for oxidation of transition metals like Fe(II) to Fe(III) followed by their rapid microbial or abiotic reduction to Fe(II) when night or high tide restores the anoxic condition.[149-151]

The oxidation of Fe(II) by O_2 in aqueous solution is stoichiometric with respect to the production of Fe(III) and superoxide[152] (Figure 3.1). Superoxide is the conjugate base of the hydroperoxyl radical, a weak acid with a pKa of 4.83.[50] Superoxide may react with several different forms of organic matter, or it may react with additional Fe(II) or undergo dismutation; either of the latter two pathways are efficient sources of hydrogen peroxide. The kinetics of the direct reaction between hydrogen peroxide and organic matter are generally slow, but it is capable of rapidly reacting with Fe(II) to yield Fe(III), hydroxyl radical and hydroxide ion. This manifold of reactions is expected at sites where oxygen-limited, Fe(II)-containing waters mix with oxygenated waters. Since the production of ROS is dependent on the Fe and oxygen dynamics of the system, the ROS profile is expected to reflect the iron and oxygen variations. Enhanced circulation of seawater through marsh sediment and/or direct gas exchange through roots should promote ROS production in pore water rich in reduced iron. Here we present the results from field studies conducted in the

South Carolina coastal marsh to test the hypothesis that the naturally occurring injection of DO into reducing sediment in the rhizosphere supports abiotic production of ROS.

3.3 Experimental Methods

Sampling Sites

The field studies were conducted in the highly-urbanized Folly creek watershed in Folly Beach, South Carolina (August 2015, March 2016 and May 2016) and at the protected North Inlet watershed in Georgetown, South Carolina (September 2015). Sample sites were at creek edges in the lower marsh where sediments were alternately inundated and exposed twice daily with the diurnal tides (Figures 3.2 and 3.3). Surface sediments remained saturated at low tide, but water continued to flow out of the creek banks after the sediment surface was exposed. Flow was observed along small channels in the creek bank, out of layers below the base of the plant roots and from burrows. At low tide, deep cracks appeared in the sediments but later closed as sediments were inundated with the rising tide. Samples were collected in the upper sediment column, well above the water table, precluding a deep groundwater source for the observed flow. Flora at both sites was dominated by *Spartina alterniflora* (marsh grass). Both sites have minimal input of fresh water from nearby rivers. Permeable layers of sand and/or shell hash were common at both sites and could support rapid horizontal flow of water in and out of the upper 50 cm of the marsh sediment. The Folly creek watershed is bounded entirely by saline water sources from the Folly River connection to the Ocean at the Stono River inlet to the East and South, the intercoastal waterway to the West, and Charleston harbor to the North. Fresh water inputs are primarily due to local precipitation leading to minimal variation in salinity during a tidal cycle. Similar to the Folly system, the Stono River receives little or no freshwater

input other than that generated by the runoff in the watershed.[153] Salinities at the sample sites were fairly constant during each sampling period and ranged from low of 28 ppt in March with higher values ranging from 31 to 33 ppt in August. The total area of the watershed is 33 km^2 with around 74% of the water cover consisting of bay/estuary and non-forested wetlands.[153] On the southeastern side of the watershed, the barrier island of Folly beach is the main land formation.

North Inlet is a tidally driven watershed located in Georgetown, South Carolina, about 80 km north of Charleston. The system is a saline and well mixed salt marsh of approximately 32 km^2 with a salinity range of 23–24 PPT during the Fall sampling period. The eastern boundary at the North Inlet is formed by barrier islands. The water cover includes about 43% of forested wetlands and 29% of estuarine emergent wetland. The inlet has an open connection to the ocean that supports active exchange of water and particulates with the ocean.[154]

Pore Water Sample Collection

Pore water samples were collected from inundated sediments during both rising and falling tides, typically with from 10 to 40 cm of overlying water during collection. Figure 3.6a provides a pictorial representation of how samples were collected in the rhizosphere, in burrows and in mud away from the plant stalk. Pore water samples were withdrawn with an acid washed syringe attached to a titanium push point sampler with silicone tubing. One sample was collected in a surface crack in the mud as it refilled on a rising tide (cracks had no water when they formed following exposure). Sediments remained saturated following exposure. However, capillary tension in the exposed sediments resulted in an apparent drop in porosity as evidenced by the appearance of deep cracks in surface sediments at low tide.

Pore water could not be extracted from exposed sediment using the push point sampler even immediately after exposure apparently due to the porosity change. Cracks appeared in the sediments within ~1 h of exposure and were attributed to capillary tension rather than evaporation due to the rapid formation of cracks coincident with low tide even during periods of very cold temperatures. Samples were collected at depths ranging from near surface to ~35 cm. The role of the *Spartina* rhizosphere was explored by varying sample points from adjacent to stems to a distance of 2 m. A small volume of pore water was collected and discarded to purge the line of any air bubbles to prevent the introduction of outside oxygen into the samples. Samples were filtered in line through Acrodisc 25-mm glass fiber filters (1 µm) before analysis for hydrogen peroxide, superoxide and iron. In line filters were flushed with pore water before data collection. The filtered samples were transferred to acid washed glass vials by slowly filling from bottom up to minimize the introduction of oxygen and were analyzed immediately following collection. Replicate oxygen measurements were made on the pore water sample that had the lowest measured oxygen. Measurements were made before sample filtering and again after filtering, splitting for analysis and preservation to evaluate a procedural blank for possible oxygen contamination during handling. The procedural blank was 5 µM, comparable to the measured oxygen concentration for the sample with the lowest oxygen concentration (4 µM).

Dissolved Oxygen (DO)

A four-channel fiber optic oxygen meter (Pyroscience Firesting O_2 FSO2-0x) coupled with bare fiber oxygen minisensors (OXB430) was used to make dissolved oxygen (DO) measurements in pore water samples for two of the Folly Beach sampling campaigns.

The sensor was calibrated using air saturated sea water (100% O_2) and sea water flushed with nitrogen (0% O_2). Sample vials were filled from the bottom and flushed with unfiltered groundwater immediately prior to analysis.

Iron Analysis

Fe(II) and Fe(III) were determined colorimetrically using the Ferrozine method.[155] The detection limit was determined to be 0.4 µM (as three times the standard deviation of the baseline measurement). The filtered pore water samples were added to vials pre-loaded with Ferrozine (1:1 volume), and absorbance measurements were taken immediately. Fe(III) analyses were carried out upon returning to the laboratory.

Hydrogen Peroxide

Hydrogen peroxide was measured by a modified acridinium ester chemiluminescence technique using a continuous flow instrument with a photomultiplier (PMT) detector (Waterville Analytical) after Cooper et al.[156] Filtered sample and the reagents were continuously pumped through a flow cell and chemiluminescence resulting from the reaction of the hydroperoxyl anion and acridinium ester at pH 12 was monitored. The wavelength maximum for the chemiluminescence occurs ~470 nm, well away from NOM absorption bands. A detection limit of 60 nM was determined (as three times the standard deviation of the baseline measurement). The samples were mixed in line with 200 mM diethylenetriaminepentaacetic acid (DTPA) prior to analysis to inhibit precipitation of $Mg(OH)_2$ and render Fe species kinetically inaccessible to further redox reactions on the timescale of the measurement. Acridinium ester and a pH modifier were then added through sequential mixing tees to initiate the photoluminescence reaction when the sample entered the detector cell. The system was recalibrated for each sample by the method of

standard addition for the analysis to minimize any possible matrix effects. The system was also externally calibrated against hydrogen peroxide standards. Hydrogen peroxide standards used for both standard additions and external calibration were themselves periodically standardized based on the absorbance at 254 nm. A typical calibration curve is shown in Figure 3.4.

Superoxide

Superoxide was determined by a chemiluminescence technique based on the reaction between superoxide and 2-methyl-6-[p-methoxyphenyl]-3,7-dihydtoimidazo[1,2-a]pyrazin-3-one (MCLA).[157,158] The MCLA reagent was prepared immediately prior to use at 5 µM in 50 mM sodium acetate buffered at pH 6. Filtered pore water was pumped into a mixing tee where the transition metals were stabilized by reaction with a 200 mM DTPA solution immediately before superoxide concentration in each sample was determined by the method of standard additions. The detection limit was less than 0.1 nM (as three times the standard deviation of the baseline measurement). Superoxide standard solutions were prepared fresh by adding potassium superoxide to 0.01 M KOH and quantified using UV absorbance at 240 and 260 nm correcting for H_2O_2 present. A background correction was carried out to account for the background signal due to MCLA autoxidation (Hansard et al. 2010). A representative calibration curve is shown in figure 3.5.

3.4 Results

DO, Fe(II), H_2O_2 and Superoxide in Sediment Pore Water

Figure 3.6a, d shows the measured pore water constituents around the grass roots and sediment of the two field sites in 2015. Dissolved Fe(II) and H_2O_2 were measured in

August, and $O_2^{\cdot-}$ was also measured for the September campaign. At both sampling sites, pore waters showed ROS (as H_2O_2) concentrations that reached levels greater than eight micromolar. The high concentration ROS samples occurred both in shallow and deep pore waters and were typically associated with higher levels of dissolved Fe(II), suggesting a possible relationship via Fe(II) oxidation (see Fig. 3.1). The measurement of DO was included the following year to explore this hypothesis. Figure 3.6b, c shows the variations in DO, Fe(II) and $O_2^{\cdot-}$ concentrations around the grass roots in the Folly salt marsh measured during the two field campaigns in 2016.

Hydrogen peroxide was also measured during both campaigns, but the detector used for H_2O_2 measurement was found to be leaking during the analysis in March; thus, those data were deemed unreliable. Surface water oxygen was also measured and was near saturation in March and ranged from ~70 to 100% oxygen saturated (167–245 µM) in May. The range in May reflected diurnal and/or tidal differences for the two sampling periods, rising tide during the late afternoon (219–245 µM), and falling tide after sunset (167–202 µM). For the March 2016 pore water samples, the general trend was decreasing DO with increasing depth for samples collected along the plant stalk, but the DO was still near 50% saturation in the deepest sample (Fig. 3.6b). In contrast, the deep pore waters samples collected 5–10 cm away from the plant stalk were typically lower. Similar trends were observed in May 2016 for pore waters collected on both the falling and rising tides, but with overall lower concentrations of DO on the rising tide. The deepest samples collected 5–15 cm away from the center of the plant stalk in May showed the lowest DO samples measured. Overall, there was a general trend of decreasing DO with depth (Figure 3.7). The DO measurement of 4 µM recorded for the 30 cm depth sample in May 2016 was

considered to be within the uncertainty of the sampling method due to the procedural blank. The Fe(II) distribution generally showed a negative correlation with DO (Fig. 3.8). This was especially true for May samples where high Fe(II) in the range of 39–70 µM were found in the near anoxic deep root system. Similarly, when DO was greater than 50% saturation, Fe(II) was near or below detection limit (dl = 1.8 µM). The relationship was expected as Fe(II) can undergo rapid oxidation in the presence of molecular oxygen. Compared to Folly creek samples in August and May, March 2016 samples contained less Fe(II), especially in the deeper root system. High Fe(II) samples with concentrations in the excess of 30 µM were all recorded at rising tide. During the May 2016 trip, pore water samples collected from similar depths at falling tide had comparatively lower Fe(II) than the rising tide samples.

Collectively the superoxide concentrations varied between 2 and 32 nM (Figure 3.6). Though there were no clear concentration gradients with depth (Figure 3.9), the highest superoxide concentrations were typically present in the deeper sediment. This was true for both September 2015 and May 2016 data sets (Fig. 3.6c, d). No clear relationship between the instantaneous concentrations of superoxide with Fe(II) or DO levels was observed. This lack of correlation was consistent with a system where the Fe(II) and oxygen levels were maintained by mass transport rather than serving as stoichiometric reservoirs for superoxide production. Higher levels of H_2O_2 were present at greater depths for the Folly marsh samples. The North Inlet samples extracted ~5 cm belowground had H_2O_2 levels exceeding 1 µM. The concentration of H_2O_2 correlated positively ($r^2 = 0.94$) with the instantaneous concentration of Fe(II) (Figure 3.10). The positive slope of the relationship indicated that Fe(II) was (net) more important as a source of H_2O_2 than as a

sink. This correlation was constant regardless of the sampling depth and the relative location of marsh grass to the sampling site.

3.5 Discussion

The correlation between Fe(II) and H_2O_2 concentrations (Figure 3.10) was consistent with the non-photochemical pathway connecting Fe(II) oxidation and H_2O_2 production depicted in Figure 3.1. The observed deficit in ^{224}Ra compared to its parent in the sediment core indicated one mechanism for mass transport of DO into the root zone was via physical forcing of pore water exchange.[77, 101,123,159-162] Sediment porosity appeared to decrease with falling tide as the marsh sediments came under capillary tension, and increase as the rising tide inundated sediments, consistent with pore collapse from surface tension and gravitational compression. The fluctuations observed in Fe(II) and ROS levels during rising and falling tides were consistent with compressible sediments. Thus, the redox state of the sediment column may have been governed by processes leading to oscillations in sediment porosity as well as varying exchange with and along roots and burrows. This process is presented conceptually in Fig. 3.11. The vertical exchange is shown to be facilitated by a high permeability layer of shell hash just below the root zone. These layers were observed at all sampling sites and are thought to facilitate water (and O_2) exchange on both rising and falling tides. This conceptual model is supported by results presented by Dias *et.al.* showing the maximum in the $^{224}Ra/^{228}Th$ disequilibrium in the deepest core sections for samples at the Folly site.[81]

An important DO source to the rhizosphere that should be independent of pore water exchange rates is O_2 gas transport across the leaf surface and into root pore spaces.

Studies have shown that a portion of the transported oxygen can diffuse through the root wall to the surrounding sediment and dissolve in pore water.[119, 138-140] The pore water samples collected from the upper 15 cm of sediment were more oxygenated compared to samples further down the root network (>25 cm), but the deep sediment zone (>25 cm) still contained oxygen. While a distinction is made for samples collected away from the center of the plant, the extent of the rhizosphere influence probably included these samples. The oxygen dispersion likely extended beyond the central plant stalk and the width of the redox zone covered a wider area around the fibrous root network. Relatively higher DO concentrations were recorded for water samples extracted in March compared to May. In March, temperatures were comparatively lower, and microbial activity is typically lower in cooler conditions.[141-143] Another qualitative indicator of a supply of DO to the deep portions of the rhizosphere was visually observed during sediment core collection for measurement of $^{224}Ra/^{228}Th$ disequilibrium. Brown-/ orange-colored vertical channels interspersed with gray to black sediments were noted down the length of the core indicating the deep distribution Fe(III) rich zones in the rhizosphere in close proximity to reduced Fe phases. These brown/orange zones were presumably generated via oxidation of dissolved or particulate Fe(II) phases. The gray to black zones was assumed to be FeS phases generated as a result of microbial sulfate reduction in the presence of Fe phases. These observations suggest cycling between oxidized and reduced Fe phases as sediment redox conditions shift with tidal variations, a process consistent with the generation of ROS. The oxidation of FeS_2 has been shown to generate ROS in laboratory experiments,[163] and the oxidation sulfide in the presence of amorphous Fe phases shows similar results.[20,21] The observed pore water conditions may reflect a metastable state during redox cycling. The

observed mixture of dissolved Fe(II), O_2, superoxide and hydrogen peroxide reported in Figure 3.2 was thermodynamically unstable. Two possible explanations for the observed mixture were that (a) the mixture was thermodynamically unstable, but the Fe(II) was sequestered from redox chemistry by a stabilizing natural ligand, or (b) the mixture was kinetically reactive but external sources of reductive equivalents reduced Fe(III) quickly to regenerate Fe(II), resulting in apparent steady-state condition. This was tested by the injection of an anthropogenic stabilizing ligand, DTPA, into the pore water, part way through the pore water analysis. The addition of the DTPA resulted in the immediate loss of the ambient hydrogen peroxide signal and superoxide signal (Figure 3.12). The loss of the peroxide and superoxide signal was consistent with loss of production via Fe(II). Given evidence that hydrogen peroxide production proceeded via the reaction of Fe(II) with DO, the magnitude of DO transport into the sediments was a possible limiting factor for ROS production in sediments.

Model Estimate of Superoxide and Hydrogen Peroxide Production Rates

In a previous study,[81] the advective exchange of pore water and overlying water constituents was carried out on a core collected adjacent to a *Spartina* stalk at the Folly site. Here, the sediment-bound inventories of ^{224}Ra and ^{228}Th in the upper 25 cm of the sediment column were considered to be at steady state with respect to particulate inputs or losses on the timescale of several ^{224}Ra half-lives ($t_{1/2}$ = 3.6 days). The steady-state assumption allows the calculation of the loss of ^{224}Ra activity due to export as Eq. (3.1) below (after Cai *et al.* 2014).[113]

The rate of 224Ra export (as activity) was estimated by:

$$F_{Ra}=\lambda_{224Ra}(A_{228Th}-A_{224Ra}) \qquad \text{Eq 3.1}$$

Where F_{Ra} is the loss of sediment ^{224}Ra activity, in excess of decay, expressed as pore water ^{224}Ra export in disintegrations per minute (dpm) of ^{224}Ra cm^{-2} day^{-1}. λ_{224Ra} is the decay constant for ^{224}Ra (0.189 day^{-1}), and A_{228Th} and A_{224Ra} are the activities of ^{228}Th and ^{224}Ra in units of dpm per gram of sediment.

The export of ^{224}Ra activity (F_{Ra}) as pore water flux was estimated using a pore water ^{224}Ra activity of 10 dpm L^{-1}. The F_{Ra} for the core yielded a pore water exchange rate in the upper 25 cm of these sediments of ~ 50 L m^{-2} day^{-1}. This is equivalent to a 10% change in the porosity in upper sediment column between periods when the sediments are inundated versus exposed. The core collection was not coincident with the pore water sampling; but was used to estimate an upper limit on DO mass transport associated with overlying water exchange in the upper sediment column in this marsh system.

The estimated water exchange rate of 54 L m^{-2} day^{-1} was used to estimate the maximum Fe(II) oxidation that could have occurred based on DO mass transfer. Assuming DO was at saturation (~250 µM) in water circulated during exchange, a 1:1 stoichiometry for Fe(II) oxidation yielded a maximum estimate of 13.5 x 10^{-3} mol m^{-2} day^{-1}. This estimate also implied a maximum associated ROS production (as superoxide) on the same order. This upper limit does not reflect the possible contribution from root/pore water O_2 exchange nor does it provide an estimate of the production of other ROS species. A simple ROS production model was generated based on the known reaction rates for Fe(II) with superoxide and Fe(II) with hydrogen peroxide. The assumption that superoxide and hydrogen peroxide production had achieved steady state in the system was also tested. The second-order rate constants for these reactions in the appropriate pH range are k_1 = 1 x 10^7 M^{-1} s^{-1} and k_{Fenton} = 2.34 x 10^4 M^{-1} s^{-1}.[11,4] The model was iteratively based on data obtained

from 60 measurements obtained at a frequency of 120 Hz. The duration was a function of the limited amount of pore water for each sample. Concentrations of Fe(II) required to maintain the observed steady-state superoxide levels for the measured time period (t) were calculated based on initial Fe(II) measurements and measured superoxide concentration at each time step.

The assumption of steady state was tested by comparing predicted consumption for each time step based on ambient conditions versus observed changes in the superoxide inventory. The signal for superoxide typically showed minimal decay over the course of the measurement (e.g., Figure 3.12 prior to the addition of DTPA). Because the initial Fe(II) concentrations were in large excess compared to superoxide, the Fe(II)/$O_2^{\cdot -}$ reaction was assumed to be pseudo first order with respect to Fe(II). Thus, the half-life was given by (Eq 3.2):

$$t_{half} = \frac{\ln 2}{k_1 [Fe^{2+}]_0} \qquad \text{Eq 3.2}$$

where $[Fe^{2+}]_0$ was the initial measured Fe(II) concentration and $k_1 = 1 \times 10^7\ M^{-1}\ s^{-1}$.[4] The predicted half-lives for superoxide were on the order of the time step (0.004–0.035 s), confirming the necessity of a steady-state condition over the course of the measurement. The assumption of steady state allows the calculation of a minimum superoxide production over the measured time period. Samples where superoxide production would be oxygen limited ([Fe(II)] > $[O_2]$) were not included in the model results. Superoxide dismutation was not included in the calculations, because the second-order reaction rate for the superoxide reaction with Fe(II) is ~125 times greater than the dismutation rates for the range of pH (7.8–8.1) measured in the overlying waters.[11,164,165] The superoxide production

necessary to balance the consumption due to reaction with ambient Fe(II) to form H_2O_2 is given by (Eq. 3.3):

$$\frac{d[O_2^{\cdot-}]}{dt} = -\frac{d[Fe(II)]}{dt} = k_1[Fe^{2+}][O_2^{\cdot-}] \qquad \text{Eq 3.3}$$

where $[Fe^{2+}]$ was the initial measured Fe(II) concentration, $[O_2^{\cdot-}]$ was the average measured superoxide concentration and $k_1 = 1 \times 10^7\ M^{-1}s^{-1}$.[11] The estimated production rates of superoxide in these pore waters ranged from ~10 to > 100 micromoles min^{-1}. Assuming that the observed superoxide inventory was maintained by the oxidation of Fe(II) and the consumption of superoxide proceeded via reaction with Fe(II) to form H_2O_2, then Fe(II) should have been limiting over the timescale of the individual measurements. The data suggest that as DO was introduced into pore water containing reduced Fe(II), the subsequent oxidation of Fe(II) led to the abiotic, nonphotochemical generation of ROS. The data also suggested that Fe(II) was resupplied to the pore water via Fe(II)/Fe(III) cycling in this system. Organic carbon-rich marine sediments can be rich in reduced sulfur species produced by the anaerobic microbial reduction of sulfates. These reduced sulfur groups drive the rapid reduction of soluble Fe(III) complexes to Fe(II).[12,13,166-168] Further Fe(II) can be generated through direct microbial reduction of Fe(III) complexes.[169-172] Within the Fe cycle, Fe(III) can undergo one electron reduction by superoxide to produce Fe(II).[1,20,173] These processes collectively lead to the regeneration of Fe(II) in the marsh sediment water column and enable Fe species to act as catalysts for ROS generation. It was surprising that measurable DO persisted over the timescale of the pore water collection periods (> 1 h see Fig. 3.6). The possible role of root/pore water O_2 exchange was considered in the context of DO mass transport during pore water exchange. The exchange of ~54 L m^{-2} day^{-1} from above would yield a DO mass transport of 13.5 mmol of DO per

day. This could be compared to DO consumption in pore waters below a single plant (assuming a distribution of one plant per square meter). Using a rough area estimate of the rhizosphere for one plant of ~0.25 m^2, then a 10 cm depth section of sediment with a porosity of 0.7 (from previous measurements) had a volume of pore water of ~18 L. Taking the minimum Fe(II) consumption estimate above at 12 micromole min^{-1} (Table 3.1) for 18 L yielded ~216 micromole DO demand per minute. Even if the majority of water exchange occurred around plants, then the total daily DO mass transfer could maintain the minimum observed superoxide production for a little more than an hour in a 10 cm sediment horizon. Thus, a significant portion of the observed superoxide production must have been maintained by another source of DO, probably root/pore water O_2 exchange in this system. This process was likely to be a critical step in the generation of additional ROS in the rhizosphere.

The observed correlation Fe(II) and H_2O_2 in these waters suggested that the production of $HO^{\cdot}$ should have occurred in these pore waters via Fenton chemistry. Based on measured concentration of Fe(II) and H_2O_2, an estimate of the production of $HO^{\cdot}$ via the Fenton reaction could be calculated. The steady-state assumption for H_2O_2 was tested in a manner similar to that used for superoxide (Eq. 3.4):

$$t_{1/2} = \frac{\ln 2}{k_F [Fe^{2+}]_0} \qquad \text{Eq 3.4}$$

where $[Fe^{2+}]_0$ was the initial measured Fe(II) concentration and k_F = 2.34 x 10^4 M^{-1} s^{-1} (Gonzales-DaVila et al. 2005).[4]

The estimated half-lives of hydrogen peroxide in the majority of samples were < 16 s, which suggested H_2O_2 concentrations were maintained at steady state as well as superoxide. The product of the superoxide consumption via reaction with Fe(II) calculated

above in Eq. 3.3 was H_2O_2. Thus, under the steady-state assumption, H_2O_2 production equaled superoxide consumption and:

$$\frac{d[H_2O_2]}{dt} = -\frac{d[O_2^{\cdot-}]}{dt} = k_1[Fe^{2+}][O_2^{\cdot-}] \qquad \text{Eq 3.5}$$

where $[Fe^{2+}]$ was the initial measured Fe(II) concentration, $[O_2^{\cdot-}]$ was the average measured superoxide concentration and $k_1 = 1 \times 10^7\ M^{-1}\ s^{-1}$.[11] If Fe(II) was not limiting, then H_2O_2 production was on the same order as the superoxide production, an assumption that seemed to be supported by the correlation observed in Figure 3.10.

While the model results demonstrated the production of H_2O_2 in pore water, it is important to note that this production could be balanced by an array of consumption reactions including but not limited to Fenton-type reactions. These pathways may also include reactions with a variety of sulfur species as well as enzymes.

Studies on salt marsh cordgrass report that *Spartina* species have peroxidase enzymes in their root systems.[174,175] The presence of enzymes to break down H_2O_2 is an important adaptation of these plants to overcome peroxide toxicity, which suggests that marsh grasses are prone to exposure to high levels of H_2O_2. Peroxidase enzymes in roots also provide a partial explanation to the rapid consumption of H_2O_2 when Fe is removed from the system. It is possible that peroxidase consumes the H_2O_2 among other organic and inorganic species in the pore water that reacts with H_2O_2. In addition, a number of soil and water microorganisms have enzymes with catalase activity which are capable of decomposing H_2O_2.[176,177]

Estimated Upper Limit for Hydroxyl Radical Production

Hydroxyl radical production rates for each of the samples were calculated based on the measured concentrations of Fe(II), H_2O_2, and the bimolecular rate constant for the Fenton reaction (k_F, 2.34 x 10^4 $M^{-1}s^{-1}$)[4] (Eq. 3.6):

$$\frac{d[HO^{\cdot}]}{dt} = k_F[Fe^{2+}][H_2O_2] \qquad \text{Eq 3.6}$$

The hydroxyl radical production rates calculated with the above rate expression varied between 1.2 x 10^{-5} and 1.7 x 10^{-9} M s^{-1} (Table 3.2). These results were on the order of laboratory studies of the non-photochemical ROS generation pathway in natural waters.[16-18,178] A detailed multivariate laboratory study of iron cycling by Burns et al. quantified $HO^{\cdot}$ generated in a Fe cycling process under typical environmental conditions.[16] In that work, the authors measured the production of hydroxyl radicals as a function of five different factors including Cl^-, Br^-, I^-, total carbonate and natural organic matter (NOM) at varying levels bracketing the conditions similar to that encountered in salt marsh systems where the field campaigns were conducted. Based on their measurements, the experimental $HO^{\cdot}$ production rates varied in the range between 1.7 x 10^{-5} and 2.0 x 10^{-7} M s^{-1}.

The range for the hydroxyl radical production rates predicted using field measurements (Table 3.2) were in good agreement with the range calculated using the experimental values reported by Burns *et. al.*[16] The field samples with $HO^{\cdot}$ production rates below the lower limit of reported laboratory rates by Burns *et. al.* all had Fe(II) levels lower than that used in the laboratory study (< 18 μM). In the pore water matrix, both Fe(II) and H_2O_2 could undergo reactions other than Fenton, lowering the fraction of each reactant that would go onto generate $HO^{\cdot}$. However, our comparisons showed that it was possible to

make reasonable predictions about $HO^{\cdot}$ formation using a simplified model based on Fe(II) and other more stable ROS associated with the Fe cycle. Being a versatile oxidant, $HO^{\cdot}$ has the capacity to play a key role in nutrient remineralization and carbon cycling in intertidal salt marsh systems. The field measurements and the model calculations presented here show an ROS production pathway connected with Fe cycling and, in turn, demonstrate a possible mechanism for oxidation of ambient organic carbon phases alone/or in tandem with microbial processes.

3.6 Conclusion

Physical mass transport of DO and gas exchange between roots and pore water create a dynamic system where dissolved oxygen and chemical constituents are readily mixed in the low marsh. The presence of DO up to 35 cm into the sediments further signified the heightened water and DO exchange rates in the marsh sediment. Together these observations compliment the high submarine groundwater exchange rates reported by Moore et al. (2008) for North and South Carolina coastline (329 m^3 of flux per meter coastline per day). These factors reflect that marsh sediment, traditionally viewed as low permeable systems, is capable of supporting higher than expected advective flow, rapid mixing between redox zones and the resultant non-photochemical production of ROS.

Despite the high carbon and sulfur loading in the marsh system, the rhizosphere and the surrounding sediment zone appear to maintain oxic/suboxic conditions. The co-existence Fe(II) with DO indicated both rapid pore water exchange and root gas exchange which created a dynamic system where oxygenated water was continuously mixed and replenished. As oxygen was introduced to the anoxic/suboxic portion of pore water, oxygen acted as an electron acceptor to set off a suite of reactions leading to the generation of

numerous transient species. Changes in advective flow with diurnal sediment inundation led to mixing of chemical species reflecting a broad range of redox conditions over the timescales of a tidal cycle.

The high correlation observed between Fe(II) and H_2O_2 further supported the possibility for H_2O_2 and by extension other ROS to be generated via a non-photochemical pathway. Model calculations show the non-photochemical pathway can make a significant contribution to the overall ROS inventories in these systems. The production of $HO^{\cdot}$ within oxic/ anoxic mixing zones in sediments emphasizes its potential for the oxidation of organic carbon in these systems. The results indicate that grass-dominated salt marsh sediments are an efficient reactor which support the net degradation of terrestrial organic matter via both ROS-based and biotic pathways.

Table 3.1: Modeled superoxide production rates based on the second order reaction between Fe(II) and superoxide observed in the pore water samples.

Initial Fe(II) (µM) measured	Measured superoxide (nM)	Superoxide production rate (µM per minute)
2.0	7	8
3.6	20	42
4.9	4	12
18.4	17	191
4.3	2	6
2.9	32	56
6.4	16	58
2.3	13	18
14.3	3	27

Table 3.2: The percentage of H_2O_2 undergoing Fenton chemistry calculated for different pore water samples based on H_2O_2 production and Fenton reaction rates.

H_2O_2 production rate (μMs^{-1})	H_2O_2consumption rate via Fenton (μMs^{-1})	% H_2O_2 in Fenton
0.57	0.011	1.96
0.97	0.013	1.35
4.45	0.16	3.58
0.13	0.003	2.55
0.017	0.002	10.07
0.71	0.047	6.65

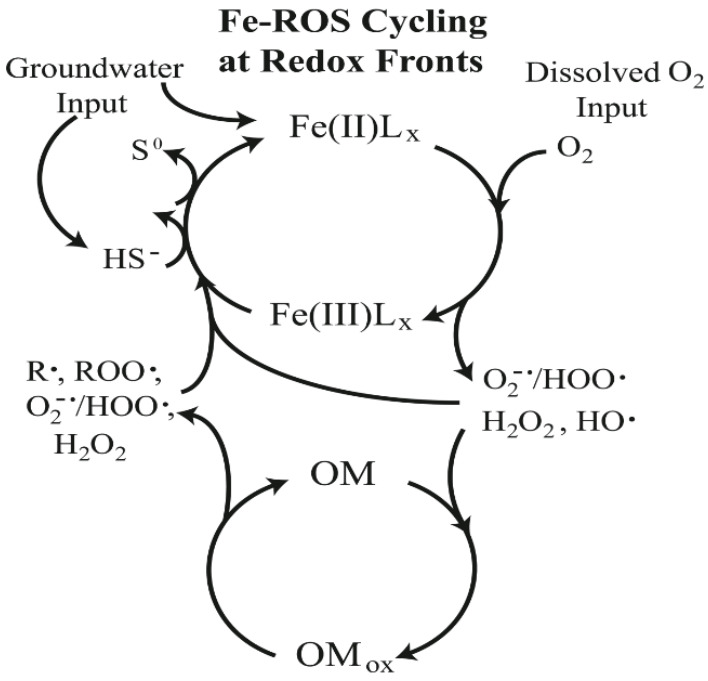

Figure 3.1: Fe-ROS cycling at redox fronts in natural waters.

Figure 3.2: Sampling site (low tide and high tide) at Folly Beach watershed in Charleston, SC.

Figure 3.3: Sampling site (low tide) at North Inlet watershed in Georgetown, SC.

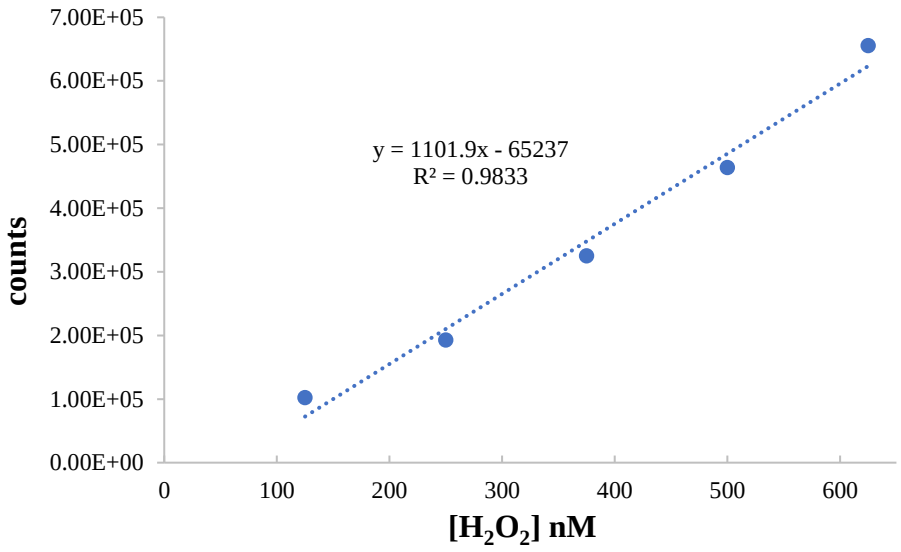

Figure 3.4: A representative calibration curve for H_2O_2 analysis by the acridinium ester method.

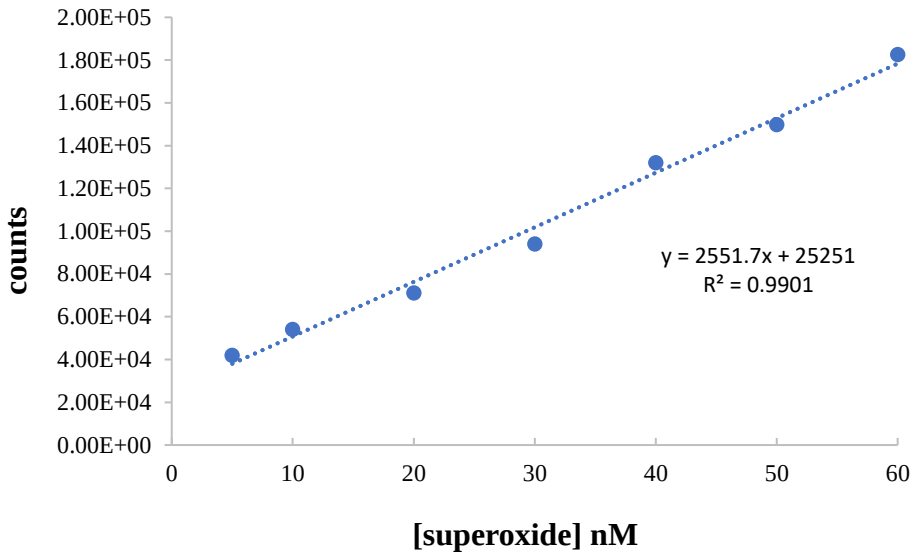

Figure 3.5: A representative calibration curve for superoxide analysis by MCLA method.

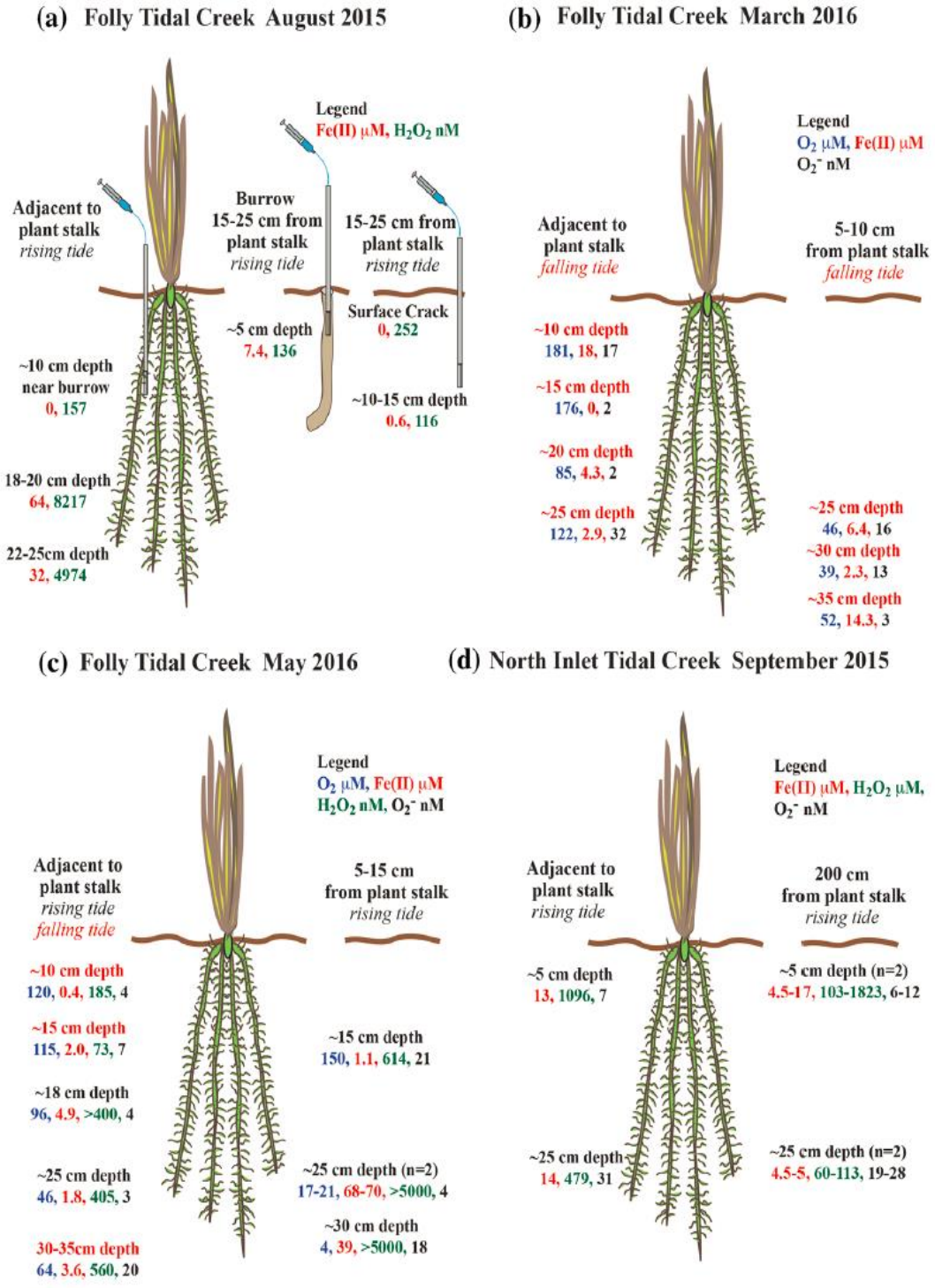

Figure 3.6(a-d): Concentrations of pore water constituents of samples collected during four field campaigns. For samples collected during rising tide, the sampling depths are shown in black and falling tide in red. Concentrations of Fe(II) and H_2O_2 in samples collected in August 2015 (2a) from 14:00-16:20, concentrations of Fe(II), H_2O_2 and $O_2^{\cdot-}$ in pore water samples collected September 2015 (2b) samples were collected from 12:00-13:30, concentrations of Fe(II), DO, and $O_2^{\cdot-}$ in pore water samples collected in March 2016 (2c) samples were collected from 11:30-12:22, and concentrations of Fe(II), DO, H_2O_2 and $O_2^{\cdot-}$ in pore water samples collected in May 2016 (2d) rising tide samples were collected from 15:45-16:50, falling tide samples were collected between 21:15 and 22:25.

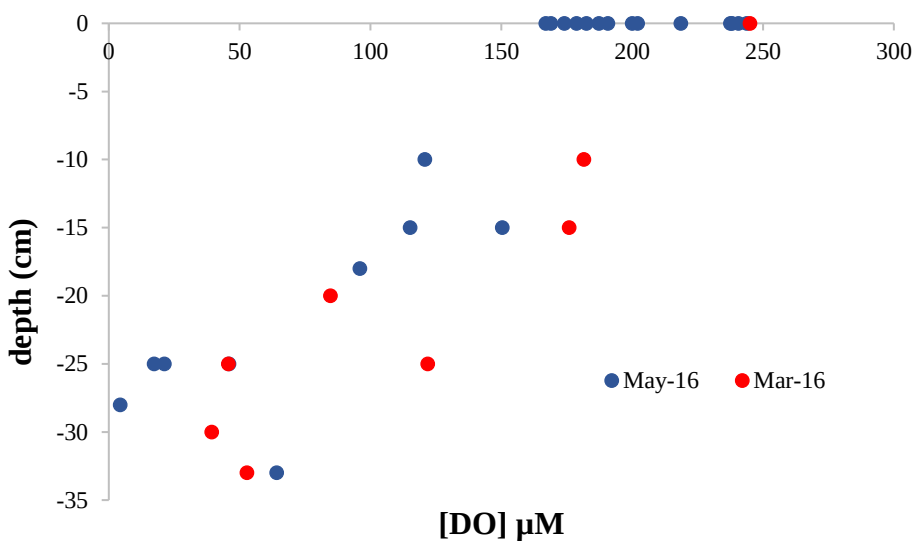

Figure 3.7: Variation in DO concentrations in pore water with sampling depth during two sampling trips at Folly Beach in March and May 2016.

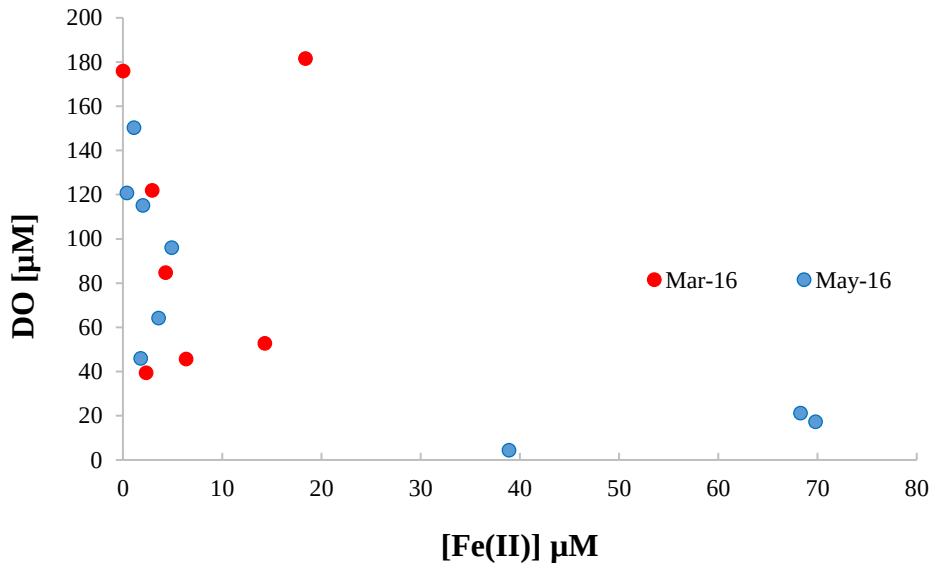

Figure 3.8: Variation in DO concentrations with pore water Fe(II) levels during two sampling trips at Folly Beach in March and May 2016.

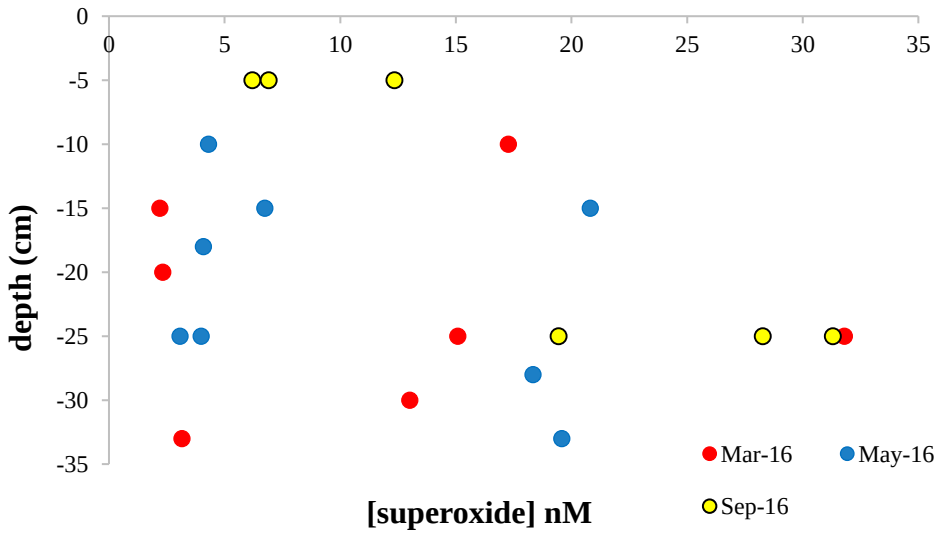

Figure 3.9: Variation in superoxide concentrations in pore water with sampling depth during three sampling trips at Folly Beach in March and May 2016 and North Inlet Creek in September 2016.

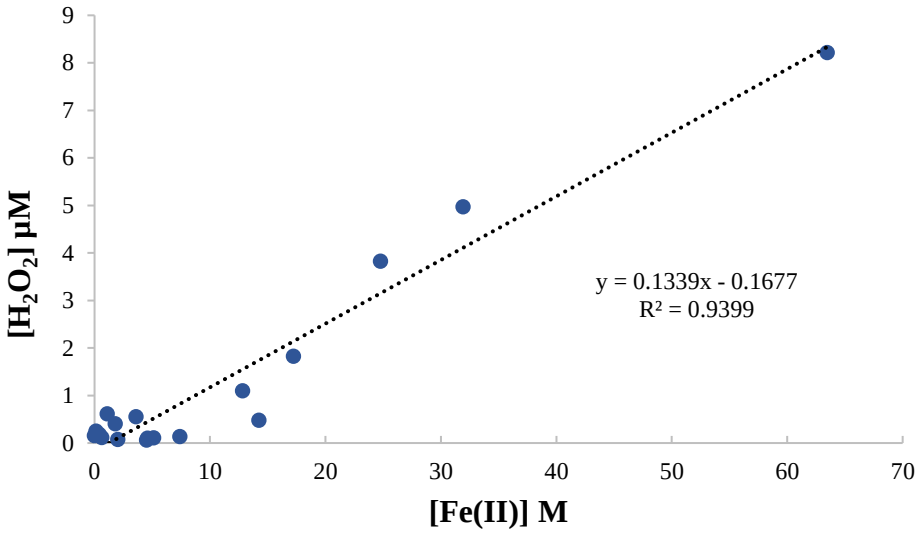

Figure 3.10: Variation in measured H_2O_2 and Fe(II) concentrations of pore water samples.

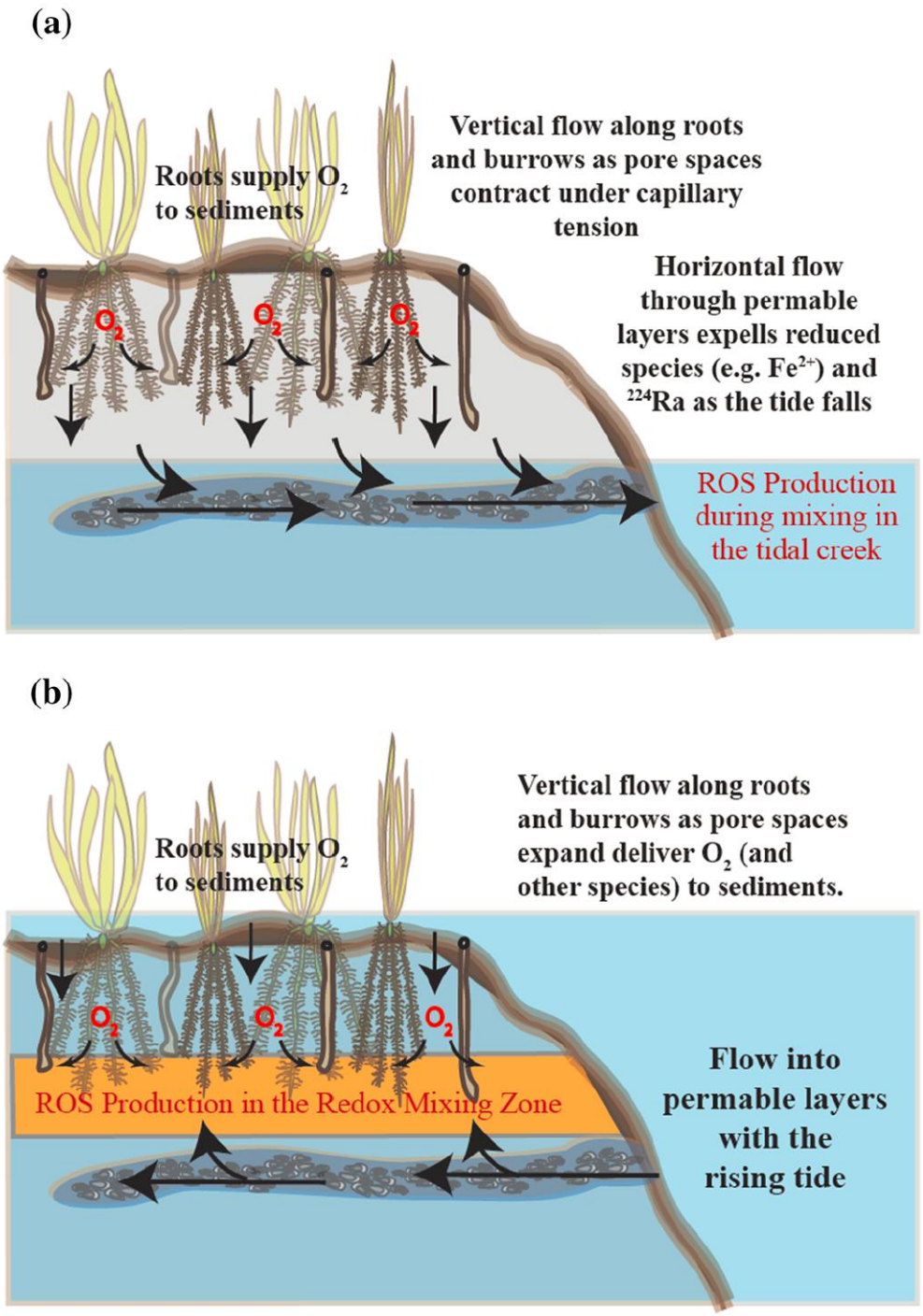

Figure 3.11: Conceptual representation of pore water exchange processes in the creek bank based on the $^{224}Ra/^{228}Th$ disequilibrium measurements and direct observations a) sediments are exposed twice daily b) sediments inundated twice daily.

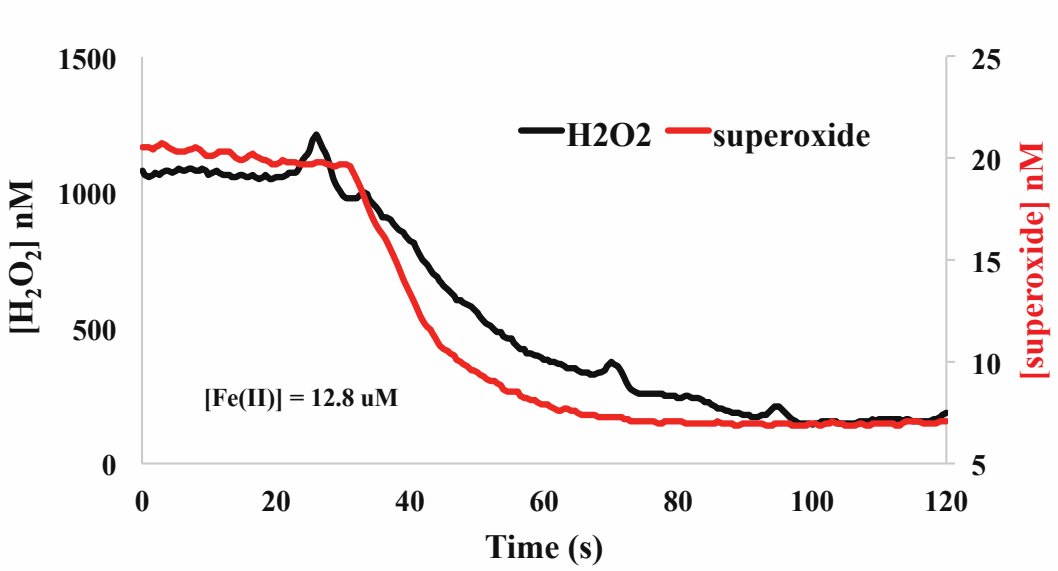

Figure 3.12: Pore water hydrogen peroxide and superoxide before and after the addition of DTPA (~t=30sec). Sample from the Baruch field site collected adjacent to a grass stalk at a depth of 5 cm in the sediment.

REFERENCES

1. King, D.W. and Farlow, R. (2000) Role of carbonate speciation on the oxidation of Fe(II) by H_2O_2. *Mar Chem.* **70**, 201-209.

2. Santana-Casiano, J.M., Gonzales-Davila, M. and Millero, F.J. (2006) The role of Fe(II) species on the oxidation of Fe(II) in natural waters in the presence of O_2 and H_2O_2. *Mar Chem.* **99**, 70-82.

3. Miller, C.J., Rose, A.L. and Waite, T.D. (2009) Impact of natural organic matter on H_2O_2 mediated oxidation of Fe(II) in a simulated freshwater system. *Geochimica Cosmochimica Ac.* **73**, 2758-2768.

4. Gonzales-DaVila, M., Santana-Casiano, J.M. and Millero, F.J. (2005) Oxidation of iron (II) nanomolar with H_2O_2 in seawater. *Geochim Cosmochim Ac.* **69**(1), 83-93.

5. Roy, A.G., Wells, M.L. and King, D.W. (2008) Persistence of Fe(II) in surface waters of the western subarctic Pacific. *Limnol Oceanogr.* **53**(1), 89-98.

6. Zee, C., Raaphorst, W. and Helder, W. (2002) Fe redox cycling in Iberian continental margin sediments (NE Atlantic). *J Mar Res.* **60**, 855-886.

7. Kustka, A.B, Shaked, Y., Milligan, A.J., King, D.W. and Morel, F.M.M. (2005) Extracellular production of superoxide by marine diatoms: Contrasting effects on iron redox chemistry and bioavailability. *Limnol Oceanogr.* **50**(4), 1172-1180.

8. Street, J.H. and Paytan, A. (2005) Iron, phytoplankton and growth and the carbon cycle. *Met Ion Biol Syst.* **43**, 153-193.

9. Boyd, P.W. and Ellwood. M.J. (2010) The biogeochemical cycle of iron in the ocean. *Nat Geosci.* **3**, 675-682.

10. Hutchins, D.A. and Boyd, P.W. (2016) Marine phytoplankton and changing ocean iron cycle. *Nat Clim Change* **6**, 1072-1079.

11. Rush, J.D. and Bielski, B.H.J. (1985) Pulse radiolytic studies of the reactions of HO_2/O_2^- with Fe(II)/Fe(III) ions. The reactivity of HO_2/O_2^- with ferric ions its implication on the occurrence of the Haber-Weiss reaction. *J Phys Chem.* **89**, 5062-5066.

12. Taillefert, M., Hover, V.C., Rozan, T.F., Theberge, S.M. and Luther III, G.W. (2002) The influence of sulfides on soluble Organic-Fe(III) in anoxic sediment porewaters. *Estuaries.* **25**(6), 1088-1096.

13. Carey, E. and Taillefert, M. (2005) The role of soluble Fe(III) in the cycling of iron and sulfur in coastal marine sediments. *Limnol Oceanogr.* **50**(4), 1129-1141.

14. Pignatello, J.J., Oliveros, E. and Mackay, A. (2006) Advanced organic processes for organic contaminant destruction based on the Fenton reaction and related chemistry. *Crit Rev Env Sci Tec.* **36**, 1-84.

15. Rose, A.L. and Waite, T.D. (2006) Role of superoxide in the photochemical reduction of iron in seawater. *Geochim Cosmochim Ac.* **70**, 3869-3882.

16. Burns, J.M., Craig, P.S., Shaw, T.J. and Ferry, J.L. (2010) Multivariate examination of Fe(II)/Fe(III) cycling and consequent hydroxyl radical generation. *Environ Sci Technol.* **44**, 7226-7231.

17. Burns, J.M., Craig, P.S., Shaw, T.J. and Ferry, J.L. (2011a) Short term Fe cycling during Fe(II) oxidation: Exploring joint oxidation and precipitation with a combinatorial system. *Environ Sci Technol.* **45**, 2663-2669.

18. Burns, J.M., Craig, P.S., Shaw, T.J. and Ferry, J.L. (2011b) Combinatorial parameter space as an empirical tool for predicting water chemistry: Fe(II) oxidation across a watershed. *Environ Sci Technol.* **45**, 4023-4029.

19. Miller, C.J., Lee, S.M.V., Rose, A.L. and Waite, T.D. (2012) Impact of natural organic matter on H_2O_2 mediated oxidation of Fe(II) in coastal sea waters. *Environ Sci Technol.* **46**(20), 11078-11085.

20. Murphy, S.A., Solomon, B.M., Meng, S., Copeland, J.M., Shaw, T.J. and Ferry, J.L. (2014) Geochemical production of reactive oxygen species from biogeochemically reduced Fe. *Environ Sci Technol.* **48**, 3815-3821.

21. Millero, F.J., and Izaguirre, M. (1989) Effects of ionic strength and ionic interactions on the oxidation of Fe(II). *J Solution Chem.***18**(6), 585-599.

22. Emmenegger, L., King, D.W., Sigg, L. and Sulzberger, B. (1998) Oxidation kinetics of Fe(II) in a eutrophic Swiss lake. *Environ Sci Technol.* **32**, 2990-2996.

23. King, D.W. (1998) Role of carbonate speciation on the oxidation rate of Fe(II) in aquatic systems. *Environ Sci Technol.* **32**, 2997-3003.

24. Rose, A.L. and Waite, D. (2002) Kinetic model for Fe(II) oxidation in sea water in the absence and presence of natural organic matter. *Environ Sci Technol.* **36**, 433-444.

25. Santana-Casiano, J.M., Gonzales-Davila, M. and Millero, F.J. (2005) Oxidation of nanomolar levels of Fe(II) with oxygen in natural waters. *Environ Sci Technol.* **39**, 2073-2079.

26.Voelker, B.T. and Sedlak, D.L. (1995) Iron reduction by photoproduced superoxide in seawater. *Mar Chem.* **50**, 93-102.

27. King, D.W., Lounsbury, H.A. and Millero, F.J. (1995) Rates and mechanism of Fe(II) oxidation at nanomolar total iron concentrations. *Environ Sci Technol.* **29**(3), 818-824.

28.Wolfenden, B.S. and Wilson, R.B. (1982) Radical-cations as reference chromogens in kinetic studies of ono-electron transfer reactions: pulse radiolysis studies of 2,2'-azinobis-(3-ethylbenzthiazoline-6-sulfonate). *J Chem Soc Perk T 2.* **7**, 805-812.

29. Mabury, S.A. and Crosby, D.G. (1996) Pesticide reactivity toward hydroxyl and its relationship to field persistence. *J Agric Food Chem.* **44**(7), 1920-1924.

30. Onstein, P. Stefan, M.I. and Bolton, J.R. (1999) Competition kinetics method for the determination of hydroxyl radicals with organic pollutants using the UV/H_2O_2 advanced oxidation technology: The rate constants for the tert-butyl formate ester and 2,4-dinitrophenol. *J Adv Oxid Technol.* **4**(2), 23 1-236.

31. Samuni, A. Goldstein, S., Russo, A., Mitchell, J.B., Krishna, M.C. and Neta, P. (2002) Kinetics and mechanism of hydroxyl radical and OH adduct radical reactions with nitroxides and with their hydroxylamines. *J Am Chem Soc.* **124**(29), 8719-8724.

32. Kwon, B.G., Ryu, S. and Yoon, J. (2009) Determination of hydroxyl radical rate constants in a continuous flow system using competition kinetics. *J Ind Eng Chem.* **15**,809-812.

33. Acero, J.L., Benitez, F.J., Real, F.J. and Roldan, G. (2010) Kinetics of aqueous chlorination of some pharmaceuticals and their elimination from water matrices. *Water Res.* **44**, 4158-4170.

34. Gebicki, J.L., Miesner, P., Stawowska, K. and Gebicka, L. (2012) Pulse radiolysis study of the reactions of catechins with nitrogen dioxide. *Radiat Phys Chem.* (12), 1881-1884.

35. Wang, P., He, Y-L. and Huang, C-H. (2011) Reactions of tetracycline antibiotics with chlorine dioxide and free chlorine. *Water Res.* **45**, 1838-1846.

36. Song, D. Liu, H., Qiang, Z. and Qu, J. (2014) Determination of rapid chlorination rate constants by a stopped-flow spectrophotometric competition kinetics method. *Water Res.* **55**, 126-132.

37. Jongberg, S., Lund, M.N., Pattison, D.I., Skibsted, L.F. and Davies, M.J. (2016) Competitive kinetics as a tool to determine rate constants for reduction of ferrylmyoglobin by food componets. *Food Chem.* **199**, 36-41.

38. Walling, C. and Kato, S. (1971) Oxidation of alcohols by Fenton's reagent. Effect of copper ion. 93(17), 4275-4281.

39. Sedlak, D.L. and Andren, A.W. (1991) Aqueous-phase oxidation of polychlorinated biphenyls by hydroxyl radicals. *Environ. Sci. Technol.* **25**, 1419-1427.

40. Haag, W.R. and Yao, C.C.D. (1992) Rate constants for reaction of hydroxyl radicals with several drinking water contaminants. *Environ. Sci. Technol.* **26**, 1005-1013.

41. Kolthoff, I.M. and Medalia, A.I. (1949) The reaction between ferrous iron and peroxides. I. Reaction with hydrogen peroxide in the absence of oxygen. *J Am Chem Soc.* **71**(11), 3777-3783.

42. Kolthoff, I.M. and Medalia, A.I. (1949) The reaction between ferrous iron and peroxides. II. Reaction with hydrogen peroxide in the presence of oxygen. *J Am Chem Soc.* **71**(11), 3784-3788.

43. Lee, T.S., Kolthoff, I.M. and Leussing, D.L. (1948) Reactions of ferrous and ferric ions with 1,10-Phenanthroline. I. Dissociation constants of ferrous and ferric phenanthroline. *J Am Chem Soc.* **70**(7), 2348-2352.

44. Adhikamsetty, R.K., Gollapalli, N.R. and Jonnalagadda, S.B. (2007) complexation kinetics of Fe^{2+} with 1,10-Phenanthroline forming ferroin in acidic solutions. *Int J Chem Kinet.* **40**(8), 515-523.

45. Lee, T.S., Kolthoff, I.M. and Leussing, D.L. (1948) Reactions of ferrous and ferric ions with 1,10-Phenanthroline. III. The ferrous monophenanthroline complex and the colorimetric determination of phenanthroline. *J Am Chem Soc.* **70**(11), 2173-2177.

46. Cagle Jr., F.W. and Fredrick Smith, G. (1947) 2,2'-bipyridine ferrous complex ion as indicator in the determination of iron. *Anal Chem.* **19**(6), 384-385.

47. Baxendale, J.H. and George, p. (1950) The kinetics of the formation and dissociation of the ferrous tris-dipyridyl ion. *T Faraday Soc.* **46**, 736-744.

48. Heaney, S.I. and Davidson, W. (1977) The determination of ferrous iron in natural waters with 2,2'-bipyridyl. *Limnol Oceanogr.* **22**(4), 753-760.

49. Tamura, H., Goto, K., Yotsuyanagi, T. and Nagayama, M. (1974) spectrophotometric determination of iron(II) with 1,10-Phenanthroline in the presence of large amounts of iron(III). *Talanta.* **21**, 314-318.

50. Bielski, B.H.J. (1978) Reevaluation of spectral and kinetics properties of HO_2 and O_2^- free radicals. *Photochem Photobiol.* **28**(4-5), 645-649.

51. Thompsen, J.C. and Mottolo, H.A. (1984) Kinetics of the complexation of Fe(II) with ferrozine. *Anal Chem.* **56**(4), 755-757.

52. Murphy, S.A., Meng, S., Solomon, B.M., Dias, D.M.C., Shaw, T.J. and Ferry, J.L. (2016) Hydrous ferrous oxides in sediment catalyze the formation of reactive oxygen species during sulfide oxidation. *Front Mar Sci.* **3**(227), 1-12.

53. Cai, W.J. and Wang, Y. (1998) The chemistry, fluxes and sources of carbon dioxide in the estuarine waters of the Satilla and Altamaha Rivers, Georgia. *Limnol Oceanogr.* **43**(4), 657-668.

54. Cai, W.J., Wiebe, W.J., Wang, Y. and Sheldon, J.E. (2000) Intertidal marsh as a source of dissolved inorganic carbon and a sink of nitrate in the Satilla River-estuarine complex in the southeastern U.S. *Limnol Oceanogr.* **45**(8), 1743-1752.

55. Chmura, G.L., Anisfeld, S.C., Cahoon, D.R. and Lynch, J.C. (2003) Global carbon sequestration in tidal, saline wetlands soils. *Global Biogeochem Cy*. **17**(4), 1-12.

56. Borges, A.V., Delille, B. and Frankignoulle, M. (2005) Budgeting sinks and sources of CO_2 in the coastal ocean: Diversity of ecosystems counts. *Geophys Res Lett.* **32**, 1-4.

57. Duarte, C.M., Middleburg, J.J. and Caraco, N. (2005) Major role of marine vegetation on the oceanic carbon cycle. *Biogeosciences.* **2**, 1-8.

58. Bouillon, S., Borges, A.V., Castaneda-Moya, E., Diele, K., Dittmar, T., Duke, N.C., Kristensen, E., Lee, S.Y., Marchand, C., Middleburg, J.J., Rivera-Monroy, V.H., Smith III., T. and Twilley, R.R. (2008) Mangrove production and carbon sinks: A revision of global budget estimates. *Global Biogeochem Cy*. **22**(2), 1-12.

59. Hopkinson, C.S., Cai, W.J. and Hu, X. (2012) Carbon sequestration in wetland dominated coastal systems – a global sink of rapidly diminishing magnitude. *Curr Opin Env Sust.* **4**(2), 186-194.

60. Bauer, J.E., Cai, W.J., Raymond, PA., Bianchi, T.S., Hopkinson, C.S. and Regnier, P.A.G. (2013) The changing carbon cycle of the coastal ocean. *Nature*. **504**, 61-70.

61. Chmura, G.L. (2013) What do we need to assess the sustainability of the tidal salt marsh carbon sink? *Ocean Coast Manage*. **83**, 25-31.

62. Frankignoulle, M., Abril, G., Borges, A., Borges, I., Canon, C., Delille, B., Libert, E. and Theate, J.M. (1998) Carbon dioxide emission from European estuaries. *Science.* **282**(5388), 434-436.

63. Borges, A.V., Schiettecatte, L.S., Abril, G., Delille, B. and Gazeau, F. (2006) Carbon dioxide in European coastal waters. *Estuar Coast Mar Sci*. **70**(3), 375-387.

64. Hedges, J.I., Keil, R.G. and Benner, R. (1997) What happens to terrestrial organic matter in the ocean? *Org Geochem*. **27**(5/6), 195-212.

65. Raymond, PA. and Bauer, J.E. (2000) Bacterial consumption of DOC during transport through a temperate estuary. *Aquat Microb Ecol*. **22**, 1-12.

66. Abril, G., Nogueira, M., Etcheber, H., Cabecadas, G., Lemaire, E. and Brogueira, M.J. (2002) Behavior of organic carbon in nine contrasting European estuaries. *Estuar Coast Shelf S.* **54**(2), 241-262.

67. Raymond, P.A. and Bauer, J.E. (2000) Atmospheric CO2 evasion, dissolved inorganic carbon production and net heterotrophy in the York River estuary. *Limnol Oceanogr*. **45**(8), 1707-1717.

68. Wang, Z.A. and Cai, W.J. (2004) Carbon dioxide degassing and inorganic carbon export from a marsh-dominated estuary (the Duplin River): A marsh CO_2 pump. *Limnol Oceanogr*. **49**(2), 341-354.

69. Jiang, L.Q., Cai, W.J. and Wang, Y. (2008) A comparative study of carbon dioxide degassing in river and marine dominated estuaries. *Limnol Oceanogr.* **53**(6), 2603-2615.

70. Cai, W.J., Wang, Z.A. and Wang, Y. (2003) The role of marsh-dominated heterotrophic continental margins in transport of CO_2 between the atmosphere, the land-sea interface and the ocean. *Geophys Res Lett.* **30**(16), 1-4.

71. Cai, W.J. (2011) Estuarine and coastal ocean carbon paradox: CO_2 inks or sites of terrestrial carbon incineration? *Annu Rev Mar Sci*. **3**, 123-145.

72. Huettel, M. and Rusch, A. (2000) Transport and degradation of phytoplankton in permeable sediment. *Limnol Oceanogr.* **45**(3), 534-549.

73. Huettel, M., Cook, P., Janssen, F., Lavik, G. and Middleburg, J.J. (2007) Transport and degradation of a diflagellate bloom in permeable sublittoral sediment. *Mar Ecol-Prog Ser.* **340**, 139-153.

74. Wilson, A.M., Huettel, M. and Klein, S. (2008) Grain size and depositional environment as predictors of permeability in coastal marine sands. *Estuar Coast Shelf S.* **80**, 193-199.

75. Bianchi, T.S. (2011) The role of terrestrially derived organic carbon in the coastal ocean: A changing paradigm and the priming effect. *P Natl Acad Sci USA.* **108**(49), 19473-19481.

76. Blaire, N.E. and Aller, R.C. (2012) The fate of terrestrial organic carbon in the marine environment. *Ann Rev Mar Sci.* **4**, 401-423.

77. Moore, W.S. and Shaw, T.J. (2008) Fluxes and behavior of radium isotopes, barium and uranium in seven Southeastern US rivers and estuaries. *Mar Chem.* **108**, 236-254.

78. Krest, J.M., Moore, W.S., Gardner, R.L. and Morris, J.T. (2000) Marsh nutrient export supplied by groundwater discharge: Evidence from radium measurements. *Global Biogeochem Cy.* **14**(1), 167-176.

79. Osgood, D.T. and Zieman, J.C. (1998) The influence of subsurface hydrology on nutrient supply and smooth cordgrass (Spartina alterniflora) production in a developing barrier island marsh. *Estuaries.* **21**(4B), 767-783.

80. Osgood, D.T. (2000) Subsurface hydrology and nutrient export from barrier island marshes at different tidal ranges. *Wetl Ecol Manag.* **8**, 133-146.

81. Dias, D.M.C., Copeland, J.M., Milliken, C.L., Shi, X., Ferry, J.L. and Shaw, T.J. (2016) Production of reactive oxygen species in the rhizophere of a Spartina-dominated salt marsh system. *Aquat Geochem.* **22**(5-6), 573-591.

82. Leonard, L.A. and Luther, M.E. (1995) Flow hydrodynamics in tidal marsh canopies. *Limnol Oceanogr.* **40**(8), 1464-1484.

83. Lopez, F. and Garcia, M. (1998) Open-channel flow through simulated vegetation: Suspended sediment transport modeling. *Water Res.* **34**(9), 2341-2352.

84. Leonard, L.A. and Reed, D.J. (2002) Hydrodynamics and sediment transport through tidal marsh canopies. *J Coastal Res.* SI**36**, 459-469.

85. Neumeier, U. and Ciavola, P. Flow resistance and associated sedimentaory processors in a *Spartina maritima* salt-marsh. *J Coastal Res.* **20**(2), 435-447.

86. Lightbody, A.F. and Nepf, H.M. (2006) Perdiction of velocity profiles and longitudinal dispersion in emergent salt marsh vegetation. *Limnol Oceanogr.* **51**(1), 218-228.

87. Botto, F. and Iribarne, O. (2000) Contrasting effects of two burrowing crabs (*Chasmagnathus granulate* and *Uca uruguayensis*) on sediment composition and transport in estuarine environments. *Estuar Coast Shelf S.* **51**, 141-151.

88. Meile, C., Koretsky, K.M. and Cappellen, P.V. (2001) Quantifying bioirrigation in aquatic sediments: An inverse modelling approach. *Limnol Oceanogr.* **46**(1), 164-177.

89. Escapa, M., Perillo, G.M.E. and Iribarne, O. (2008) Sediment dynamics modulated by burrowing crab activities in contrasting SW Atlantic intertidal habitats. *Estuar Coast Shelf S.* **80**, 365-373.

90. Daleo, P. and Iribarne, O. (2009) The burrowing crab *Neohelice granulate* affects the root strategies of the cordgrass *Spartina densiflora* in SW Atlantic salt marshes. *J Exp Mar Biol Ecol.* **373**, 66-71.

91. Aller, R.C. and Aller, J.Y. (1998) The effect of biogenic irrigation intensity and solute exchange on diagenetic reaction rates in marine sediment. *J Mar Res.* **56**, 905-936.

92. Botto, F. Iribarne, F., Gutierrez, J., Bava, J., Gagliardini, A. and Valiela, I. (2006) Ecological importance of passive deposition of organic matter into burrows of the SW Atlantic crab *Chasmagnathus granulatus. Mar Ecol Prog Ser*. **312**, 201-210.

93. Canfield, D.E. (1994) Factors influencing organic carbon preservation in marine sediments. *Chem Geol.* **114**, 315-329.

94. Kristensen, E., Ahmad, S.I. and Devol, A.H. (1995) Aerobic and anaerobic decomposition of organic matterin marine sediment: Which is fastest? *Limnol Oceanogr*. **40**(8), 1430-1437.

95. Sun, M-Y., Wakeham, S.G. and Lee, C. (1997) Rates and mechanisms of fatty acid degradation in oxic and anoxic coastal marine sediment of Long Island Sound, New York, USA. *Geochimica Cosmochimica Ac.* **61**(2), 341-355.

96. Hartnett, H.E., Keil, R.G., Hedges, J.I. and Devol, A.H. (1998) Influence of oxygen exposure time on organic carbon preservation in continental margin sediments. *Nature*. **391**, 572-574.

97. Thullner, M., Regnier, P. and Cappellen, P.V. (2007) Modelling microbially induced carbon degradation in redox-stratified subsurface environments: Concepts and open questions. *Geomicrobiol J*. **24**(3-4), 139-155.

98. Arndt, S., Jorgenson, B.B., LaRowe, D.E., Middleburg, J.J., Pancost, R.D. and Regnier, P. (2013) Quantifying the degradation of organic matter in marine sediments: A review and synthesis. *Earth-Sci Rev.* **123**, 53-86.

99. Charette, M.A., Buesseler, K.O. and Andrews, J.E. (2001) Utility of radium isotopes for evaluating the input and transport of groundwater-driven nitrogen to Cape Cod estuary. *Limnol Oceanogr*. **46**(2), 465-470.

100. Moore, W.S. (2006) Radium isotopes as tracers of submarine groundwater discharge in Sicily. *Cont Shelf Res.* **26**, 852-861.

101. Moore, W.S., Sarmiento, J.L. and Key, R.M. (2008) Submarine groundwater discharge revealed by ^{228}Ra distribution in the upper Atlantic Ocean. *Nat Geosci.* 1, 309-311.

102. Wilson, A.M., Moore, W.S., Joye, S.B., Anderson, J.L. and Schutte, C.A. (2011) Storm-driven groundwater flow in a salt marsh. *Water Resour Res.* **47**, 1-11.

103. Hsieh, Y-T., Geibert, W., van Beek, P., Stahl, H., Aleynik, D. and Henderson, G.M. (2013) Using the radium quartet (^{228}Ra, ^{226}Ra, ^{224}Ra and ^{223}Ra) to estimate water mixing and radium inputs in Loch Evite, Scotland. *Limnol Oceanogr*. **58** (3), 1089-1102.

104. Men W., Jiang, Y., Liu, G., Wang, F. and Zhang, Y. (2016) Study of water mixing in the coastal waters of the western Taiwan Strait based on radium isotopes. *J Environ Radioact.* **152**, 16-22.

105. Hougham, A.L. and Moran, S.B. (2007) Water mass ages of coastal ponds estimated using ^{223}Ra and ^{224}Ra as tracers. *Mar Chem.* **105**, 194-207.

106. Colbert, S.L. and Hammond, D.E. (2008) Shoreline and seafloor fluxes of water and short-lived Ra isotopes to surface water of San Pedro Bay, CA. *Mar Chem.* **108**, 1-17.

107. Liu, L., Yi, L., Cheng, X. and Tang, G. (2013) Distribution of 223Ra and 224Ra in the Bo Sea embayment in Tianjin and its implication of submarine groundwater discharge. *J Environ Radioact.* **150**, 111-120.

108. Burt, W.J., Thomas, H., Patsch, J., Omar, A.M., Schrum, C., Daewel, U., Brenner, H. and Baar, H.J.W. (2014) Radium isotopes as a tracer of sediment-water column exchange in the North Sea. *Global Biogeochem Cy.* **28**(8), 786-804.

109. Garcia-Orellana, J., Cochran, J.K., Bokuniewicz, H., Daniel, J.W.R., Rodellas, V. and Heilbrun, C. (2014) Evaluation of ^{224}Ra as a tracer for submarine groundwater discharge in Long Island Sound, NY. *Geochim Cosmochim Ac.* **141**, 314-330.

110. Tamborski, J.J., Cochran, J.K. and Bokuniewicz, H. (2017) Application of ^{224}Ra and ^{222}Rn for evaluating seawater residence times in a tidal subterranean estuary. *Mar Chem.* **189**, 32-45.

111. Moore, W.S. and Arnold, R. (1996) Measurement of ^{223}Ra and ^{224}Ra in coastal waters using a delayed coincidence counter. *J Geophys Res.* **101**(C1), 1321-1329.

112. Cai, P., Shi, X., Moore, W.S. and Dai, M. (2012) Measurement of ^{224}Ra: ^{228Th} disequilibrium in coastal sediments using a delayed coincidence counter. *Mar Chem.* **138-139**, 1-6.

113. Cai, P., Shi, X., Moore, W.S., Peng, S., Wang, G. and Dai, M. (2014) ^{224}Ra: ^{228Th} disequilibrium in coastal sediments: Implications for solute transfer across the sediment-water interface. *Geochim Cosmochim Ac.* **125**, 68-84.

114. Cai, P., Shi, X., Hong, Q., Li, Q., Liu, L., Guo, X. and Dai, M. (2015) Using 224R/228Th disequilibrium to quantify benthic fluxes of dissolved inorganic carbon and nutrients into Pearl River Estuary. *Geochim Cosmochim Ac.* **170**, 188-203.

115. Rama, Todd, J.F., Butts, J.L. and Moore, W.S. (1987) A new method for the rapid measurement of ^{224}Ra in natural waters. *Mar Chem.* **22**, 43-54.

116. Moore, W.S. and Krest, J. (2004) Distribution of 223Ra and 224Ra in the plumes of the Mississippi and Atchafalaya Rivers and the Gulf of Mexico. *Mar Chem.* **86**, 105-119.

117. Sundby, B., Caetano, M., Vale, C., Gobeil, C., Luther III, G.W. and Nuzzio, D.B. (2005) Root-induced cycling of lead in salt marsh sediments. *Environ Sci Technol.* **39**, 2080-2086.

118. Colmer, T.D. (2003a) Long distance transport of gases in plants: a perspective on internal aeration and radial oxygen loss from roots. *Plant Cell Environ.* **26**, 17-36.

119. Winkel, A., Colmer, T.D. and Pederson, O. (2011) Leaf gas films of *Spartina anglica* enhance rhizome and root oxygen during total submergence. *Plant Cell Environ.* **34**, 2083-2092.

120. Rama, and Moore, W.S. (1996) Using the radium quartet for evaluating groundwater input and water exchange in salt marshes. *Geochimica Cosmochimica Ac.* **60**(23), 4645-4652.

121. Duarte, C.M., Middleburg, J.J. and Caraco, N. (2005) Major role of marine vegetation on the oceanic carbon cycle. *Biogeosciences*. **2**, 1-8.

122. Anschutz, P., Smith, T., Mouret, A., Deborde, J., Bujan, S., Poirier, D. and Lecroart, P. (2009) Tidal sands as biogeochemical reactors. *Estuar Coast Shelf S.* **84**, 84-90.

123. Wildman Jr., R.A., Chan, N.W., Dalleska, N.F., Anderson, M. and Hering, J.G. (2010) Effect of changes in water level on sediment porewater redox geochemistry at a reservoir shoreline. *Appl Geochem.* **25**, 1902-1911.

124. Belicka, L.L. and Harvey, H.R. (2009) The sequestration of terrestrial organic carbon in Arctic Ocean sediments: A comparison of methods and implications of regional carbon budgets. *Geochimica Cosmochimica Ac.* **73**, 6231-6248.

125. Watanabe, K. and Kuwae, T. (2015) How organic carbon derived from multiple sources contributes to carbon sequestration processes in a shallow coastal system? *Glob Change Biol.* **21**, 2612-2623.

126. Graham, G.W. and Manning, A.J. (2007) Floc size and settling velocity within *a Spartina angelica* canopy. *Cont Shelf Res.* **27**, 1060-1079

127. Cowie, G.L. and Hedges, J.I. (1994) Biochemical indicators of diagenetic alteration in natural organic matter mixtures. *Nature*, **369**, 304-307.

128. Shaw, T.J., Sholkovitz, E.R. and Klinkhammer, G. (1994) Redox dynamics in the Chesapeake Bay: The effect on sediment/water uranium exchange. *Geochim Cosmochim Ac*. **58**(14), 2985-2995.

129. Keil, R.G., Tsamakis, E., Giddings, J.C. and Hedges, J.I. (1998) Biochemical distributions (amino acids, neutral sugars and cupric oxide oxidation products) among size-classes of modern marine sediments. *Geochim Cosmochim Ac.* **62**, 1347-1364.

130. Aller, R.C., Madrid, V., Christoserdov, A., Aller, J.Y., and Heilbrun, C. (2010) Unsteady diagenetic processes and sulfur biogeochemistry in tropical deltaic muds: Implications for ocean isotope cycles and the sedimentary record. *Geochimica Cosmochimica Ac.* **74**, 4671-4692.

131. Cai, W-J., Luther III, G.W., Cornwell, J.C. and Giblin, A.E. (2010) Carbon cycling and the coupling between proton and electron transfer reactions in aquatic sediments in Lake Champlain. *Aquat Geochem.* **16**, 421-446.

132. Nesbitt, H.W. and Young, G.M. (1989) Formation and diagenesis of weathering profiles. *J. Geol.* **97**, 129-147.

133. Morford, J.L. and Emerson, S. (1999) The geochemistry of redo sensitive trace metals in sediments. *Geochim Cosmochim Ac.* **63**, 1735-1750.

134. Bradley, J.D. and Gerrans, G.C. (1973) Frontier molecular orbitals. A link between kinetics and bonding theory. *J Chem Educ.* **50**(7), 463.

135. Wu, J. and Luther III, G.W. (1995) Complexation of Fe(III) by natural organic ligands in the Northwest Atlantic Ocean by a competitive ligand equilibration method kinetic approach. *Mar Chem.* **50**, 150-179.

136. Rickard, D., Schoonen, M.A.A. and Luther III, G.W. (1995) Chemistry of iron sulfides in sedimentary environments. *ACS Symp Ser.* **612**, 168-193.

137. Luther III, G.W. (2004) Kinetics of the reactions of water, hydroxide ion and sulfide species with CO_2, OCS and CS_2: Frontier molecular orbital considerations. *Aquat Geochem.* **10**(1), 81-97.

138. Mendelssohn, I.A. (1995) Factors controlling the formation of oxidized root channels: A review. *Wetlands.* **15**, 37-46.

139. Colmer, T.D. (2003b) Aerenchyma and an inducible barrier to radial oxygen loss facilitate root aeration in Upland, paddy and deepwater rice (*Oryza sativa* L.). *Ann Bot.* **91**, 301-309.

140. Lee, R.W. (2003) Physiological adaptations of the invasive cordgrass *Spartina Anglica* to reducing sediments: Rhizome metabolic gas fluxes and enhanced O_2 and H_2S transport. *Mar Biol.* **143**, 9-15.

141. Holade, S.A., Martindale, W., Alred, R., Brooks, A.L. and Leegood, R.A. (1992) Changes in activites of enzymes of carbon metabolism in leaves during exposure of plants to low temperature. *Plant Physol.* **98**(3), 1105-1114.

142. Pinedo, M.L., Hernandez, G.F., Conde, R.D. and Tognetti, J.A. (2000) Effect of low temperature on the protein metabolism in wheat leaves. *Biol Plantarum.* **43**(3), 363-367.

143. Atkin, O.K. and Tjoelker, M.G. (2003) Thermal acclimation and the dynamic response of plant respiration to temperature. *Trends Plant Sci.* **8**(7), 343-351.

144. Meile, C., Koretsky, K.M. and Cappellen, P.V. (2001) Quantifying bioirrigation in aquatic sediments: An inverse modelling approach. *Limnol Oceanogr.* **46**(1), 164-177.

145. Volkenborn, N., Polerecky, L., Wethey, D.S. and Woodin, S.A. (2010) Oscillatory porewater bioadvection in marine sediments induced by hydraulic activities of *Arenicola marina*. *Limnol Oceanogr.* **55**(3), 1231-1247.

146. Sundby, B., Vale, C., Caetano, M., Catarino, F., Madureira, M-J. and Caetano, M. (1998) Metal-rich concretions on the roots of salt marsh plants: Mechanism and rate of formation. *Limnol Oceanogr.* **43**(2), 245-252.

147. Sundby, B., Vale, C., Caetano, M. and Luther III, G.W. (2003) Redox chemistry in the root zone of a salt marsh sediment in the Targus Estuary, Portugal. *Aquat Geochem.* **9**, 257-271.

148. Koretsky, C.M. and Miller, D. (2008) Seasonal influence of the Needle Rush *Juncas roemarianus* on saltmarsh porewater geochemistry. *Estuar Coast.* **31**, 70-84.

149. Hines, M.E. (1991) The role of certain infauna and vascular plats in the mediation of redox reactions in marine sediment. Berthelin, J. (Ed.), Diversity of Environmental Biogeochemistry. Elsevier, 275-286.

150. Gribsholt, B. and Kristensen, E. (2003) Benthic metabolism and sulfur cycling along an inundation gradient in a tidal *Spartina anglica* salt marsh. *Limnol Oceanogr.* **48**(6), 2151-2162.

151. Koretsky, C.M., Cappellen, P.V., DiChristina, T.J., Kostka, J.E., Lowe, K.L., Moore, C.M., Roychoudhury, A.N. and Viollier, E. (2005) Salt marsh pore water geochemistry dos not correlate with microbial community structure. *Estuar Coast Shelf S.* **62**, 233-251.

152. Wardman, P. and Candaias, L.P. (1996) Fenton Chemistry: An introduction. *Radiat Res.* **145**(5), 523-531.

153. Carter, J.B. (2010) Using geographic information systems (GIS) as a tool for characterizing the Charleston-North Charleston urbanized area to guide stormwater education and outreaching programming. Masters' thesis, Clemson University.

154. Allen, D.M., Allen, W.B., Feller, R.F. and Plunket, J.S. editors (2014) Site profile of the North Inlet-Winyah Bay National Estuarine Reserve. North Inlet-Winyah Bay National Estuarine Reserve. Georgetown, SC, 432.

155. Stookey, L.L. (1970) Ferrozine – a new spectrophotometric reagent for iron. *Anal Chem*. **42**(7), 779-781.

156. Cooper, W.J., Moegling, J.K., Kieber, R.J. and Kiddle, J.J. (2000) A chemiluminescene method for the analysis of H_2O_2 in natural waters. *Mar Chem.* **70**(1-3), 191-200.

157. Rose, A.L., Webb. E.A., Waite, T.D. and Moffett, J.W. (2008) Measurement and implications of nonphotochemically generated superoxide in the equatorial Pacific Ocean. *Environ Sci Technol.* **42**, 2387-2393.

158. Hansard, S.P., Vermilyea, A.W. and Voelker, B.M. (2010) Measurements of superoxide radical concentration and decay kinetics in the Gulf of Alaska. *Deep Sea Research I.* **57**, 1111-1119.

159. Burnett, W.C., Bokuniewicz, H., Huettel, M., Moore, W.S. and Taniguchi, M. (2003) Groundwater and pore water inputs to the coastal zone. *Biogeochemistry*. **66**(1), 3-33.

160. Smith, L. and Zawadzki, W. (2003) A hydrogeological model of submarine groundwater discharge: Florida intercomparison experiment. *Biogeochemistry*. **66**(1-2)95-110.

161. Snyder, M., Taillefert, M. and Ruppel, C. (2004) Redox zonation at the saline-influenced boundaries of a permeable surficial aquifer: effects of physical forcing on the biogeochemical cycling of iron and manganese. *J Hydrol.* **296**, 164-178.

162. Burnett, W.C., Aggarwal, P.K., Aureli, A., Bokuniewicz, H., Cable, J.E., Charette, M.A., Kontar, E., Krupa, S., Kulkarni, K.M., Loveless, A., Moore, W.S., Oberdorfer, J.A., Oliveira, J., Qzyurt, N., Povinec, P., Privitera, A.M.G., Rajar, R., Ramessur, R.T., Scholten, J., Steiglitz, T., Taniguchi, M. and Turner, J.V. (2006) Quantifying submarine groundwater discharge in the coastal zone via multiple methods. *Sci Total Environ.* **367**(2-3), 498-543.

163. Schoonen, M.A.A., Harrington, A.D., Laffers, R. and Strongin, D.R. (2010) Role of hydrogen peroxide and hydroxyl radical in pyrite oxidation by molecular oxygen. *Geochim Cosmochimica Ac.***74**, 4971-4987.

164. Bielski, B.H.J., Cabelli, D.E., Arudi, R.L. and Ross, A.B. (1985) Reactivity of HO_2/O_2^- radicals in aqueous solution. *J Phys Chem Ref Data.* **14**(4), 1041-1100.

165.Copeland, J.M. (2016) Novel approaches to investigate the oxidation rate of Fe(II) and the role of Fe(II)/Fe(III) cycling on the maintenance of reactive oxygen species in aquatic systems. Ph.D. thesis, University of South Carolina, Columbia, SC.

166. Luther III, G.W., Kostka, J.E., Church, T.M., Sulzberger, B. and Stumm, W. (1992) Seasonal iron cycling in the salt-marsh sedimentary environment; the importance of ligand complexes with Fe(II) and Fe(III) in the dissolution of Fe(III) minerals and pyrite, respectively. Mar Sci. **40**(1-2), 81-103.

167. Millero, F.J., Gonzalez-DaVila, M. and Santana-Casiano, J.M. (1995) Reduction of Fe(III) with sulfite in natural waters. *J Geophys Res.* **100**(D4), 7235-7244.

168. Yao, W. and Millero, F.J. (1996) Oxidation of hydrogen sulfide by hydrous Fe(III) oxides in seawater. *Mar Chem.* **52**, 1-16.

169. Lovley, D.R. (1991) Dissimilatory Fe(III) and Mn(IV) reduction. *Microbiol Rev.* **55**(2), 259-287.

170. Lovley, D.R., Roden, E.E., Phillips, E.J.P. and Woodward, J.C. (1993) Enzymatic iron and uranium reduction by sulfate-reducing bacteria. *Mar Geol.* **113**(1-2), 41-53.

171. Fredrickson, J.K. and Gorby, Y.A. (1996) Environmental processes mediated by iron reducing bacteria. *Curr Opin Biotech.* **7**, 287-294.

172. Dollhopf, M.E., Nealson, K.H., Simon, D.M. and Luther III, G.W. (2000) Kinetics of Fe(III) and Mn(IV) reduction by the Black Sea strain of *Shewanella putrifaciens* using in situ solid state voltammetric Ag/Hg electrodes. *Mar Chem.* **70**, 171-180.

173. Rose, A.L. and Waite, T.D. (2005) Reduction of organically complexed ferric iron by superoxide in a simulated natural water. *Environ Sci Technol.* **39**(8), 2645-2650.

174. Wall, V.D., Alberts, J.J., Moore, D.J., Newell, S.Y., Pattnayek, M. and Pennings, S.C. (2001) The effect of mercury and PCBs on organisms from lower trophic levels of a Georgia salt marsh. *Arch Environ Contam Toxicol.* **40**, 10-17.

175. Duarte, B., Almeida, P.R. and Cacador, I. (2009) Spartina maritima (cordgrass) rhizosediment extracellular enzymatic activity and its role in organic matter decomposition processes and metal speciation. *Mar Ecol.* **30**(1), 65-73.

176. Schellhorn, H.E. (1994) Regulation of hydroperoxidase (catalase) expression in *Escherichia coli*. *FEMS Microbiol Lett.* **131**, 113-119.

177. Busalmen, J.P., Vazquez, M. and de Sanchez, S.R. (2002) New evidences on the catalase mechanism of microbial corrosion. *Electrochim Acta.* 47, 1857-1865.

178. Tong, M., Yuan, S., Ma, S., Jin, M., Liu, D., Cheng, D., Liu, X., Gan, Y. and Wang, Y. (2016) Production of abundant hydroxyl radicals from oxygenation of subsurface sediments. *Environ Sci Technol.* **50**, 214-221.

APPENDIX A – PERMISSION TO REPRINT

Order Completed

Thank you for your order.

This Agreement between University of South Carolina -- Dewamunnage Muditha Dias ("You") and Springer ("Springer") consists of your license details and the terms and conditions provided by Springer and Copyright Clearance Center.

Your confirmation email will contain your order number for future reference.

printable details

License Number	4219541119699
License date	Oct 31, 2017
Licensed Content Publisher	Springer
Licensed Content Publication	Aquatic Geochemistry
Licensed Content Title	Production of Reactive Oxygen Species in the Rhizosphere of a Spartina-Dominated Salt Marsh Systems
Licensed Content Author	Dewamunnage Muditha C. Dias, Justin M. Copeland, Carrie L. Milliken et al
Licensed Content Date	Jan 1, 2016
Licensed Content Volume	22
Licensed Content Issue	5
Type of Use	Thesis/Dissertation
Portion	Full text
Number of copies	4
Author of this Springer article	Yes and you are the sole author of the new work
Order reference number	
Title of your thesis / dissertation	Investigation of iron(II) autoxidation rate and iron mediated geochemical production of reactive oxygen species at oxic-anoxic interfaces
Expected completion date	Dec 2017
Estimated size(pages)	126

Requestor Location	University of South Carolina 631 Sumter Street COLUMBIA, SC 29206 United States Attn: University of South Carolina
Billing Type	Invoice
Billing address	University of South Carolina 631 Sumter Street